

Discrete Approximation of Topologically Protected Modes in Magneto-Optical Media

Mark J. Ablowitz and Justin T. Cole¹

¹*Department of Applied Mathematics, University of Colorado, Boulder, Colorado 80309*

(Dated: February 19, 2020)

Topologically protected waves in the linearly polarized Maxwell's equations with gyrotropic/magneto-optic media were studied a decade ago both computationally and experimentally. This paper develops a robust tight-binding model for this system that makes careful use of Wannier function representations. The model provides very good approximations to the underlying band structure. When solved on a semi-infinite strip, it produces exponentially localized edge modes whose corresponding eigenvalues span the frequency band gaps. A set of coupled differential equations are derived which allows one to find how the electromagnetic field propagates unidirectionally, without backscatter from defects. Furthermore, the discrete model predicts topologically protected edge modes with nontrivial Chern number which are consistent with direct simulation.

I. INTRODUCTION

Topological insulators in photonic lattices are an exciting and active area of current research. Among the distinguished features of these systems are the presence of the topologically protected edge modes that under the right set of conditions propagate unidirectionally, without backscatter from defects. With these properties in mind there have been numerous investigations to understand the nature, key properties and scope of these topological modes cf. [1] and to understand how these states can potentially be harnessed in future applications [2, 3].

The idea of synthesizing a topological insulator within an electromagnetic system governed by Maxwell's equations was first proposed in the seminal work of Haldane and Raghu [4, 5]. In those works a transverse electric (TE) field in the presence of an anisotropic permittivity tensor with periodic structure was considered. By introducing a set of hermitian, purely imaginary, off-diagonal elements into the permittivity tensor it is possible to break time-reversal symmetry. Doing this has the effect of creating a gap at the inter-band touching points, which is filled by so-called 'gapless' topologically protected edge modes. The underlying topological structure is established by the existence of nontrivial topological invariants such as Chern numbers. The spectrum and corresponding solutions of this problem were rigorously studied in [6].

A different system, inspired by the above work of Haldane and Raghu, found transverse magnetic (TM) fields that can exhibit gapless edge states when an external magnetic field is applied to an array of ferrimagnet rods [7]. The external bias generates a magneto-optical (MO) response that manifests itself in a gyrotropic permeability tensor [8] which breaks time-reversal symmetry, but not inversion symmetry. As a result, the system possesses nontrivial Chern invariants and supports unidirectional mode propagation analogous to the quantum Hall effect [9, 10]. These modes were experimentally observed within a square lattice [11]. A similar topological insulator system that uses a honeycomb lattice instead was also found to support topologically protected modes [12, 13].

Subsequently a photonic topological insulator was in-

vestigated in [14] where an effective magnetic field was induced by the helical driving of a honeycomb waveguide in the direction of propagation. Advantages of this system are that no external magnetic field is required and the frequencies are in the optical regime. A tight binding model of this system including nonlinear effects and propagating solitons along an edge was discussed in [15]. This system has been shown to support novel topological phenomena such as Weyl points [16] and valley-hall states [17].

The purpose of this paper is to construct a tight-binding model that describes the MO system considered in [7] as well as a broad class of related problems. To our knowledge no such tight-binding system describing these type of MO systems have been found before. Tight-binding approximations produce effective, simplified discrete models; they are able to capture the essence of the system, provide important qualitative information, and relative to full numerics they are computable at a fraction of the cost. In this context we employ a novel sequence of methods that are appropriate for this application.

Here we employ a Wannier mode expansion of the electromagnetic field to derive our topological insulator model; this is different from an expansion in terms of gaussian-type orbitals. The latter, while very useful for Schrödinger operators cf. [18, 19], have not been found to be effective in this topological class of problems. The difficulty with using a direct Wannier mode expansion is that the MO system is a Chern insulator and as a result the decay rate of the Wannier functions is slow [20]. This means that a direct Wannier approach to obtain a tight-binding system for a Chern insulator (i.e. a system with nontrivial Chern numbers which occurs in this problem due to the breaking of time-reversal symmetry) presents serious obstacles.

To obtain a localized basis of modes from which to construct our discrete model we employ a *perturbative* Wannier approach whereby we obtain a set of Wannier modes from a closely related equation that *does* possess time-reversal symmetry. We find that this approximate set of Wannier modes produces spectral band diagrams which are in remarkably good agreement with numerics. From the above Wannier expansion we construct a sys-

tem of differential equations for the modal coefficients from which we compute the spectral bands and corresponding edge eigenmodes. The adjacent bulk bands are found to possess nontrivial Chern numbers which, by the bulk-edge correspondence, indicate the presence of topologically protected modes [21]. Moreover, evolution of these edge states is found to propagate unidirectionally around a lattice defect. These results are in agreement with prior MO work [7, 11, 22].

The outline of the paper is the following. In Sec. II starting from Maxwell's equations we formulate the TM equation that governs this MO system. We approximate the ferrite rods by super-Gaussian functions and represent the electric field by a Bloch wave. In Sec. II B we give a brief introduction to Wannier functions and motivate our perturbative approach. With this Wannier Galerkin-type basis in hand, the tight-binding discrete system is derived; the coefficients of the discrete model are calculated in Sec. IV and the discrete system is solved in Sec. V. There we compute the linear spectral bands for both the bulk and edge problems. The bulk bands are found to possess nonzero Chern numbers that with the bulk-band correspondence agree with the number and orientation of gapless edge modes we find. Finally, in Sec. VI direct numerical simulations are performed on the discrete model. The edge modes are found to flow unidirectionally and propagate without backscatter around lattice defects. We conclude in Sec. VII.

II. THE TM EQUATION WITH GYROTROPIC TENSOR

We start at the source-free and current-free Maxwell's equations

$$\nabla \times \mathbf{H} = \frac{\partial \mathbf{D}}{\partial t}, \quad \nabla \times \mathbf{E} = -\frac{\partial \mathbf{B}}{\partial t}, \quad \nabla \cdot \mathbf{D} = 0, \quad \nabla \cdot \mathbf{B} = 0, \quad (1)$$

where \mathbf{H} is the magnetic field, \mathbf{E} is the electric field, \mathbf{D} is the electromagnetic displacement, and \mathbf{B} is the magnetic induction. Consider a real time-harmonic electromagnetic field $\mathbf{E}(\mathbf{r}, t) = \tilde{\mathbf{E}}(\mathbf{r}, \omega)e^{i\omega t} + c.c.$, $\mathbf{H}(\mathbf{r}, t) = \tilde{\mathbf{H}}(\mathbf{r}, \omega)e^{i\omega t} + c.c.$, where *c.c.* is the complex conjugate and ω is the angular frequency.

The electric field is taken to be linearly polarized in the perpendicular z -direction and depends on the transverse variables x, y , i.e. $\tilde{\mathbf{E}}(\mathbf{r}, \omega) = (0, 0, E(\mathbf{r}, \omega))$ such that $\mathbf{r} = (x, y)$. The displacement and electric fields are related via

$$\mathbf{D}(\mathbf{r}, t) = \epsilon(\mathbf{r})\mathbf{E}(\mathbf{r}, t), \quad (2)$$

with scalar permittivity function $\epsilon(\mathbf{r})$. For a linearly polarized field this displacement vector clearly satisfies the divergence-free condition $\nabla \cdot \mathbf{D} = 0$. The function $\epsilon(\mathbf{r})$ models a square array of YIG rods ($\epsilon = 15\epsilon_0$) such as those considered in [7, 11] [see Fig. 1(b)]. A constant external magnetic field H_0 is applied in the z -direction.

For a ferrimagnetic material the external magnetic field aligns the magnetic dipoles and induces a magnetization response [8]. The magnetic induction and magnetic field are related by the gyrotropic permeability tensor

$$\tilde{\mathbf{B}} = [\mu]\tilde{\mathbf{H}}, \quad [\mu](\mathbf{r}) = \begin{pmatrix} \mu & i\kappa & 0 \\ -i\kappa & \mu & 0 \\ 0 & 0 & \mu_0 \end{pmatrix}(\mathbf{r}), \quad (3)$$

where

$$\mu = \mu_0 \left(1 + \frac{\omega_0 \omega_m}{\omega_0^2 - \omega^2} \right) \quad \text{and} \quad \kappa = \mu_0 \frac{\omega \omega_m}{\omega_0^2 - \omega^2}.$$

The frequencies above are $\omega_0(\mathbf{r}) = \mu_0 \gamma H_0(\mathbf{r})$ and $\omega_m(\mathbf{r}) = \mu_0 \gamma M_s(\mathbf{r})$, where μ_0 is the vacuum permeability, $\gamma = 1.759 \times 10^7 \text{ rad}/(\text{Gs})$ is the gyromagnetic ratio and M_s is the magnetization saturation. We point out that the relationship between the magnetic fields in (3) satisfies the divergence relation $\nabla \cdot \mathbf{B} = 0$.

For simplicity throughout this paper we assume a dispersionless tensor and fix the frequency ω in the coefficients μ and κ . The dispersive problem was considered in [7]; it did not significantly alter the structure of the spectral bands and resulting topology. We use typical physical parameters $H_0 = 1600 \text{ Oe}$ and $M_s = 1810 \text{ G}$ resulting in values of $\mu = 14\mu_0$ and $\kappa = 12.4\mu_0$ within the ferrite rods. Combining equations (1), (2), and (3) yields

$$\nabla \times ([\mu]^{-1} \nabla \times \tilde{\mathbf{E}}) = \omega^2 \epsilon \tilde{\mathbf{E}}, \quad (4)$$

where

$$[\mu]^{-1} = \begin{pmatrix} \tilde{\mu}^{-1} & i\eta & 0 \\ -i\eta & \tilde{\mu}^{-1} & 0 \\ 0 & 0 & \mu_0^{-1} \end{pmatrix},$$

such that $\tilde{\mu} = (\mu^2 - \kappa^2)/\mu$ and $\eta = -\kappa/(\mu^2 - \kappa^2)$. For a linearly polarized field we obtain the following ‘‘master’’ equation

$$-\nabla^2 E + [\nabla \ln \tilde{\mu} - i\tilde{\mu}(\hat{\mathbf{z}} \times \nabla \eta)] \cdot \nabla E = \omega^2 \epsilon \tilde{\mu} E. \quad (5)$$

This equation is non-dimensionalized by

$$\mathbf{r} = a\mathbf{r}', \quad \mu = \mu_0 \mu', \quad \kappa = \mu_0 \kappa', \quad \epsilon = \epsilon_0 \epsilon', \quad \omega = \frac{c}{a} \omega',$$

where $c = 1/\sqrt{\mu_0 \epsilon_0}$ is the speed of light in vacuum and a is the distance between two adjacent lattice rods. The non-dimensionalized master equation (after dropping the ' notation) is

$$-\nabla^2 E + \mathcal{M}(\mathbf{r}) \cdot \nabla E = \omega^2 \epsilon \tilde{\mu} E, \quad (6)$$

$$\mathcal{M}(\mathbf{r}) \equiv \nabla \ln \tilde{\mu} - i\tilde{\mu}(\hat{\mathbf{z}} \times \nabla \eta).$$

In the frequency domain, the imaginary term in Eq. (6) is responsible for breaking time-reversal symmetry. As we will see below, this term leads to bands with nontrivial Chern numbers and gapless edge modes.

A. Periodic Lattice

The ferrite rods in the non-dimensionalized lattice are taken to have period 1 in the transverse plane. The corresponding lattice vectors are

$$\mathbf{e}_1 = (1, 0), \quad \mathbf{e}_2 = (0, 1). \quad (7)$$

Starting from the origin, the location of the rods are integer multiples of the lattice vectors, given by $\mathbf{R}_{mn} \equiv m\mathbf{e}_1 + n\mathbf{e}_2$, where $m, n \in \mathbb{Z}$. The locations given by \mathbf{R}_{mn} correspond to the centers of the lattice rods below; which we later refer to as the integer lattice sites. Both the permittivity and permeability tensors possess this periodic structure, hence they exhibit the following translation invariance

$$\begin{aligned} \epsilon(\mathbf{r} + \mathbf{R}_{mn}) &= \epsilon(\mathbf{r}), & \mu(\mathbf{r} + \mathbf{R}_{mn}) &= \mu(\mathbf{r}), \\ \kappa(\mathbf{r} + \mathbf{R}_{mn}) &= \kappa(\mathbf{r}). \end{aligned}$$

To model a single YIG rod of the lattice we use the following super-Gaussian function

$$l(x, y) = \exp \left[- \left(\frac{\sqrt{x^2 + y^2}}{\delta} \right)^6 \right]. \quad (8)$$

This function approximates a cylindrical rod of radius 0.11 considered in [7]. To make the two functions comparable we choose the parameter δ so that the half width at half maximum of (8) is equal to the radius of the cylindrical rods; this yields $\delta = 0.11/(\log 2)^{1/6}$. To obtain band diagrams that are close those found using a pure cylinder, it is important this function has a sharp derivative.

To model an array of rods we form a series of super-Gaussians centered at the integer lattices sites. The explicit functions we use are

$$\begin{aligned} \epsilon(\mathbf{r}) &= 1 + 14 \sum_{m,n} l(x - m, y - n), \\ \mu(\mathbf{r}) &= 1 + 13 \sum_{m,n} l(x - m, y - n), \\ \kappa(\mathbf{r}) &= 12.4 \sum_{m,n} l(x - m, y - n). \end{aligned} \quad (9)$$

A profile comparison between a cylindrical rod and the super Gaussian in (8) is shown in Fig. 1(a). A plot of the arrays in (9) is shown in Fig. 1(b). These periodic arrays are used to compute the Bloch modes discussed in the next section. In turn, the Bloch modes are used to directly compute bands and the Wannier functions.

B. Numerical Computation of Bloch Eigenfunctions

Consider the sourceless eigenvalue problem in (6) with periodic coefficients. Solutions are Bloch modes of the form

$$E_p(\mathbf{r}, \mathbf{k}) = e^{i\mathbf{k}\cdot\mathbf{r}} u_p(\mathbf{r}, \mathbf{k}), \quad u_p(\mathbf{r} + \mathbf{R}_{mn}, \mathbf{k}) = u_p(\mathbf{r}, \mathbf{k}), \quad (10)$$

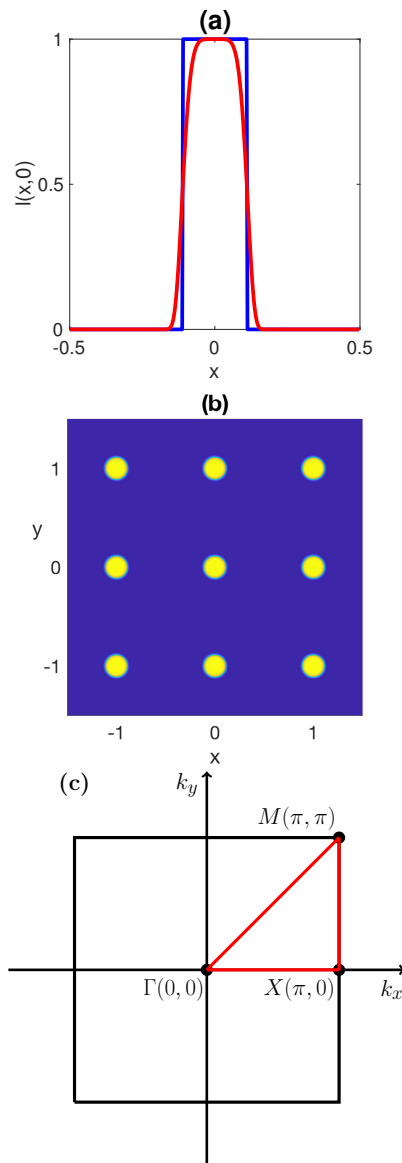


FIG. 1. (color online) (a) Super-Gaussian profile (red curve) given in (8) in comparison to cylinder of radius 0.11 profile (blue curve). (b) Square array of super-Gaussian rods. (c) First Brillouin zone (BZ) of the square lattice: $[-\pi, \pi] \times [-\pi, \pi]$. The irreducible Brillouin zone is the triangular region with vertices Γ, X, M .

where p denotes the corresponding band number and $\mathbf{k} \equiv (k_x, k_y)$ is the 2D quasimomentum. This then gives

$$- (\nabla + i\mathbf{k})^2 u_p + \mathcal{M}(\mathbf{r}) \cdot (\nabla + i\mathbf{k}) u_p = \omega^2(\mathbf{k}) \epsilon(\mathbf{r}) \tilde{\mu}(\mathbf{r}) u_p. \quad (11)$$

Since the function $u_p(\mathbf{r}, \mathbf{k})$ is periodic in \mathbf{r} it can be expanded in the Fourier series

$$u_p(\mathbf{r}, \mathbf{k}) = \sum_{m,n} \hat{u}_{p,mn}(\mathbf{k}) e^{i\mathbf{G}_{mn}\cdot\mathbf{r}}, \quad (12)$$

where $\mathbf{G}_{mn} \equiv 2\pi m\mathbf{e}_1 + 2\pi n\mathbf{e}_2$, $m, n \in \mathbb{Z}$. The effective permittivity and permeability functions are also periodic

and expanded in terms of Fourier series:

$$(\epsilon\tilde{\mu})(\mathbf{r}) = \sum_{m,n} (\widehat{\epsilon\tilde{\mu}})_{mn} e^{i\mathbf{G}_{mn}\cdot\mathbf{r}},$$

$$\mathcal{M}(\mathbf{r}) = \sum_{m,n} \widehat{\mathcal{M}}_{mn} e^{i\mathbf{G}_{mn}\cdot\mathbf{r}}.$$

For this spectral method to be effective the potential in (9) needs to be smooth enough that the Fourier coefficients decay sufficiently rapidly. On the other hand, the magnetic term $\mathcal{M}(\mathbf{r})$ in (6) needs to be strong enough (i.e. have a large enough gradient) to open a sufficiently large gap. We find that the super-Gaussian in (8) is a compromise between these opposing sides. For the Bloch modes computed in this paper we took 40 Fourier modes and a spatial discretization of $\Delta x = \Delta y = 1/240$.

Eigenvalue problem (11) is transformed into the coupled, algebraic system of equations

$$(\mathbf{G}_{mn} + \mathbf{k})^2 \widehat{u}_{p,mn}(\mathbf{k}) \quad (13)$$

$$+ i \sum_{m',n'} \widehat{\mathcal{M}}_{m'n'} \cdot (\mathbf{G}_{m-m',n-n'} + \mathbf{k}) \widehat{u}_{p,m-m',n-n'}(\mathbf{k})$$

$$= \omega^2(\mathbf{k}) \sum_{m',n'} (\widehat{\epsilon\tilde{\mu}})_{m'n'}(\mathbf{k}) \widehat{u}_{p,m-m',n-n'}(\mathbf{k}),$$

where $(\mathbf{G} + \mathbf{k})^2 \equiv |\mathbf{G}|^2 + 2\mathbf{G} \cdot \mathbf{k} + |\mathbf{k}|^2$. Eigenvalue

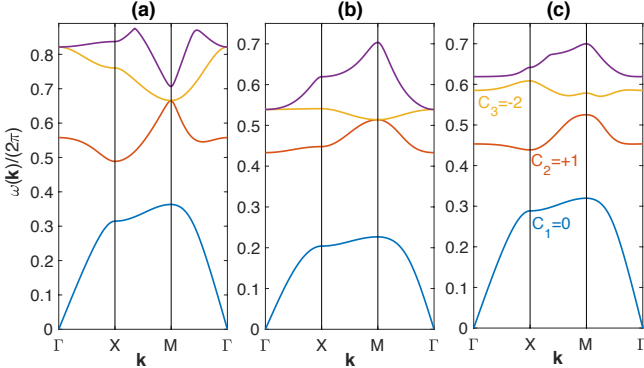


FIG. 2. First four dispersion bands in ascending order. Values of \mathbf{k} are taken along the perimeter of the irreducible zone in Fig. 1. Bands are computed from (11) using parameters: (a) $\tilde{\mu} = 1, \mathcal{M}(\mathbf{r}) = \mathbf{0}$, (b) $\tilde{\mu}$ defined in (4) and (9), $\mathcal{M}(\mathbf{r}) = \mathbf{0}$, and (c) $\tilde{\mu}$ defined in (4) and (9), $\mathcal{M}(\mathbf{r}) \neq \mathbf{0}$. The computed Chern numbers defined in (14) for the corresponding bands are included in (c).

problem (13) is solved numerically for all \mathbf{k} in the first Brillouin zone (BZ) given by $[-\pi, \pi] \times [-\pi, \pi]$. After solving (13), the Fourier coefficients $\widehat{u}_{p,mn}(\mathbf{k})$ are returned to the series (12) and summed to give the Bloch wave. The Bloch modes are normalized by fixing $\iint_{\text{UC}} |E_p(\mathbf{r}, \mathbf{k})|^2 \epsilon(\mathbf{r}) \tilde{\mu}(\mathbf{r}) d\mathbf{r} = 1$, where UC denotes the unit cell $[-1/2, 1/2] \times [-1/2, 1/2]$.

The eigenvalue equation in (11) always contains spatial inversion symmetry since it is invariant under the transformations $\mathbf{k} \rightarrow -\mathbf{k}$ and $\mathbf{r} \rightarrow -\mathbf{r}$, and as a result the spectrum exhibits the inversion symmetry $\omega(\mathbf{k}) = \omega(-\mathbf{k})$.

When $\mathcal{M}(\mathbf{r}) \neq \mathbf{0}$ time reversal symmetry is broken; i.e. the imaginary term in (6) prevents the equation coming back to itself when $\mathbf{k} \rightarrow -\mathbf{k}$ and the complex conjugate of the equation is taken.

First we numerically solve (13) in the absence of any magnetic field. In Fig. 2(a) the first four dispersion bands are found to consist of two subsets: the (isolated) first band and the (touching) second through fourth bands. The band touching points occur at the origin (Γ) and corner (M) of the Brillouin zone. Next we consider an intermediate magnetized case that will play a crucial role in deriving our tight-binding system below. To obtain the bands in Fig. 2(b) we solve (11) with $\mathcal{M}(\mathbf{r}) = \mathbf{0}$, but $\tilde{\mu} \neq 0$ on the right-hand side of the equation. Again, the second, third, and fourth bands are all entangled, however this is still a system with time-reversal symmetry (and hence well-localized Wannier modes). We observe that our numerically obtained eigenfunctions $\widehat{u}_{mn}(\mathbf{k})$ are real in this case.

Finally we compute the fully magnetized problem ($\mathcal{M}(\mathbf{r}) \neq \mathbf{0}$) and display the bands in Fig. 2(c). Importantly, time-reversal symmetry has been broken and a gap has opened between the second and third bands, as well as between the third and fourth bands. It is within these newly formed gaps we later find topologically protected edge modes when a sharp edge boundary is introduced. The frequency gap ranges between the second and third bands are found to be (0.525, 0.571) and between the third and fourth bands are (0.609, 0.619). These values are in good agreement with [7]. In dimensional units, a lattice constant of $a = 40\text{mm}$ means these frequency gaps correspond to (3.93, 4.28) GHz and (4.56, 4.60) GHz, respectively.

As stated above, introducing the $\mathcal{M}(\mathbf{r}) \neq \mathbf{0}$ term in (6) breaks time-reversal symmetry; in turn this generates bands with nontrivial Chern number [4, 5]. The continuous Chern number of the p^{th} spectral band is defined by

$$C_p = \frac{1}{2\pi i} \iint_{\text{BZ}} (\nabla_{\mathbf{k}} \times \mathbf{A}_p) \cdot \hat{\mathbf{z}} d\mathbf{k}, \quad (14)$$

where $\mathbf{A}_p(\mathbf{k}) = \langle u_p(\mathbf{r}, \mathbf{k}) | \partial_{k_x} u_p(\mathbf{r}, \mathbf{k}) \rangle_{\text{UC}, \epsilon\tilde{\mu}} \hat{\mathbf{x}} + \langle u_p(\mathbf{r}, \mathbf{k}) | \partial_{k_y} u_p(\mathbf{r}, \mathbf{k}) \rangle_{\text{UC}, \epsilon\tilde{\mu}} \hat{\mathbf{y}}$ is the Berry connection defined in terms of the complex inner product

$$\langle f(\mathbf{r}) | g(\mathbf{r}) \rangle_{\text{UC}, \epsilon\tilde{\mu}} = \iint_{\text{UC}} f(\mathbf{r})^* g(\mathbf{r}) \epsilon(\mathbf{r}) \tilde{\mu}(\mathbf{r}) d\mathbf{r}.$$

The numerical algorithm in [23] is used to compute (14). As indicated in Fig. 2(c) the second and third bands acquire a nontrivial Chern number; which agrees with those found in [7]. The bulk-edge correspondence indicates that topologically protected edge modes can be found in the band gaps when an edge boundary is introduced [21]. Topologically protected states are calculated below in Sec. VB; they are consistent with the Chern numbers found here.

III. A PERTURBATION APPROACH TO WANNIER EXPANSION

A tight-binding model is an approximation that transforms a PDE into a system of differential equations. These approximations are most effective in deep lattice regimes where the Bloch mode can be expanded in terms of rapidly decaying basis functions centered at different spatial locations. These basis functions are sometimes referred to as Wannier modes. Approximations to Wannier modes, termed orbitals, are also frequently used. The methodology is most useful when the Wannier modes/orbitals are rapidly decaying. The overlap between rapidly decaying Wannier modes/orbitals is significant only among nearby sites and, as a result, the infinite series can be truncated to a manageable number of interactions. Typically the first few neighbors (nearest/next-nearest) are enough to gain a good approximation of the full problem.

The Bloch wave in (10) is periodic in \mathbf{k} and hence can be expanded in terms of the Fourier series $E(\mathbf{r}, \mathbf{k}) = \sum_{m,n} w_{m,n}(\mathbf{r}) \exp(i\mathbf{R}_{mn} \cdot \mathbf{k})$. The Fourier coefficients are the Wannier modes and their decay rate in \mathbf{r} depends on the smoothness of $E(\mathbf{r}, \mathbf{k})$ in \mathbf{k} . When the magnetic field $\mathcal{M}(\mathbf{r})$ in (6) is nonzero time-reversal symmetry is lost and the system acquires a nontrivial Chern number [7]. In this regime the Bloch function $E(\mathbf{r}, \mathbf{k})$ is characterized by a discontinuity in \mathbf{k} [20]. As such, the Bloch wave does not have even one full derivative throughout the Brillouin zone and consequently the direct Wannier modes decay too slowly to be useful in a tight-binding model.

Below we describe a perturbative approach to obtain a tight-binding model where the Wannier modes from a closely related equation are used to approximate the full problem. These approximate modes lead to a discrete system of differential equations that accurately describe the spectral bands. Moreover this discrete system supports a set of topologically protected modes that propagate unidirectionally around lattice defects without backscatter.

Let us motivate the perturbative approach. The essence of the method is to exploit the scales between the (relatively) weak $\mathcal{M}(\mathbf{r})$ term in comparison to the (relatively) strong effective potential $\epsilon(\mathbf{r})\tilde{\mu}(\mathbf{r})$ term in Eq. (6). Inside the lattice rods the amplitudes of the inverse permeability tensor elements in (4) are $\tilde{\mu}(\mathbf{r}) \approx 3$ and $\eta(\mathbf{r}) \approx -0.29$, while the amplitude of the effective potential is $\epsilon\tilde{\mu} \approx 45$. For the smoothed potentials in (9) the root mean squares of these magnetic terms over one unit cell are $\sqrt{\iint_{UC} |\partial_x \ln \tilde{\mu}|^2 d\mathbf{r}} = \sqrt{\iint_{UC} |\partial_y \ln \tilde{\mu}|^2 d\mathbf{r}} = 2.70$ and $\sqrt{\iint_{UC} |\tilde{\mu}\eta_y|^2 d\mathbf{r}} = \sqrt{\iint_{UC} |\tilde{\mu}\eta_x|^2 d\mathbf{r}} = 1.88$. In comparison to the strength of the effective permittivity term $\sqrt{\iint_{UC} |\epsilon(\mathbf{r})\tilde{\mu}(\mathbf{r})|^2 d\mathbf{r}} = 7.65$, the strength of these individual magnetic terms are 35% and 25%, respectively. In fact, it is the (weaker) second term that is responsible for the topological effects. Relative to the effective potential $\tilde{\mu}(\mathbf{r})\epsilon(\mathbf{r})$ these terms are small, hence inclusion of

the $\mathcal{M}(\mathbf{r})$ term in (6) can be viewed as a perturbation to the same equation when $\mathcal{M}(\mathbf{r}) = \mathbf{0}$. While this perturbation ratio is on the large side we find it does yield quite stable and accurate results.

A. Fourier-Wannier Modes

We now give a brief review of the Wannier functions and their properties. The spectrum of (6) consists of bulk dispersion surfaces, or bands, that are ordered by increasing frequency and are indexed by $p = 1, 2, \dots$. The full Bloch wave is written as a linear combination of the Bloch modes from the different bands i.e.

$$E(\mathbf{r}, \mathbf{k}) = \sum_{p=1}^{\infty} \alpha_p(\mathbf{k}) E_p(\mathbf{r}, \mathbf{k}) . \quad (15)$$

As mentioned earlier, the Bloch function is periodic in \mathbf{k} . Hence each Bloch mode is expanded in terms of a Fourier series

$$E_p(\mathbf{r}, \mathbf{k}) = \sum_{m,n=-\infty}^{\infty} w_{p,mn}(\mathbf{r}) e^{i\mathbf{k} \cdot \mathbf{R}_{mn}} , \quad (16)$$

where, under certain conditions, the Wannier coefficients are exponentially localized in space. The Wannier mode corresponding to the p^{th} band is computed directly from the Bloch mode by

$$w_{p,mn}(\mathbf{r}) = \frac{1}{4\pi^2} \iint_{\text{BZ}} e^{-i\mathbf{k} \cdot \mathbf{R}_{mn}} E_p(\mathbf{r}, \mathbf{k}) d\mathbf{k} , \quad (17)$$

where $4\pi^2$ is the area of the first Brillouin zone (BZ). The Wannier functions decay to zero as $|\mathbf{r}| \rightarrow \infty$. A key property of Wannier functions is that in a specific band they are related through integer translations. This implies

$$w_{p,mn}(\mathbf{r}) = w_{p,00}(\mathbf{r} - \mathbf{R}_{mn}) , \quad \mathbf{R}_{mn} = m\mathbf{e}_1 + n\mathbf{e}_2 . \quad (18)$$

Hence the electric field is being expanded in terms of an infinite number of copies of the same Wannier mode located at each lattice site \mathbf{R}_{mn} . We define the complex inner product

$$\langle f(\mathbf{r}) | g(\mathbf{r}) \rangle_{\mathbb{R}^2} = \iint_{\mathbb{R}^2} f(\mathbf{r})^* g(\mathbf{r}) d\mathbf{r} . \quad (19)$$

The Wannier functions form an orthogonal basis on \mathbb{R}^2 and satisfy the following orthogonality relation

$$\langle w_{\ell,m'n'} | \epsilon\tilde{\mu} w_{p,mn} \rangle_{\mathbb{R}^2} = \delta_{mm'} \delta_{nn'} \delta_{\ell p} , \quad (20)$$

where δ_{ij} is the Kronecker delta.

Due to the nature in which eigenvalue problem (11) is solved numerically there is non-uniqueness in the Bloch modes which causes discontinuities in \mathbf{k} . Since the eigenvalue problem is linear, at each value of \mathbf{k} the normalized eigenfunction is only known up to an arbitrary constant i.e. $C(\mathbf{k})E(\mathbf{r}, \mathbf{k})$. In general, the function $C(\mathbf{k})$ is not smooth which means the corresponding Wannier mode decays slowly. To improve the localization properties of

the modes from bands $p = 2, 3, 4$ we utilize the Marzari and Vanderbilt (MV) algorithm [24]. This algorithm applies a gradient descent method to find Wannier modes that minimize the spread or variance. Details of our implementation of the MV algorithm are given in Appendix A. The first band is isolated from all others in Fig. 2 and the corresponding Bloch mode is smoothed by the rescaling method described in Appendix A 1.

The numerically computed Wannier modes are shown in Fig. 3. Recall that these modes are calculated from the $\mathcal{M}(\mathbf{r}) = \mathbf{0}$ problem in (6). As a result, this equation has time-reversal symmetry and the corresponding Wannier modes are real [24]. The first, third, and fourth Wannier modes are found to be centered at the origin, whereas the second mode is centered at the off-rod, half-integer point $(-\frac{1}{2}, -\frac{1}{2})$. This somewhat surprising result that the $p = 2$ Wannier mode is centered off-site is a consequence of the optimization procedure used in the MV algorithm (see also [25]). As a final note, depending on the initial guess, sometimes these Wannier modes can appear in a different order. If this occurs, we re-order them so that off-site mode shown in Fig. 3(b) corresponds to $p = 2$.

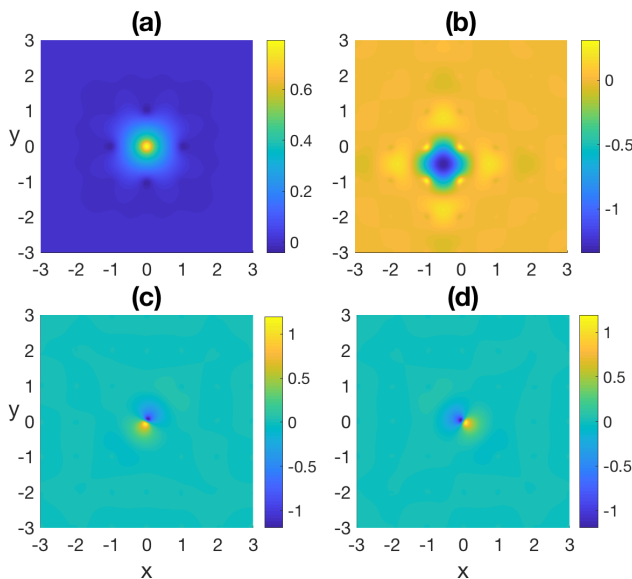


FIG. 3. Plot of Wannier modes (all from (6) with $\mathcal{M}(\mathbf{r}) = \mathbf{0}$): (a) $w_{1,00}(\mathbf{r})$, (b) $w_{2,00}(\mathbf{r})$, (c) $w_{3,00}(\mathbf{r})$, and (d) $w_{4,00}(\mathbf{r})$.

The tight-binding approximation used below is most effective when the Bloch function is expressed in terms of a rapidly decaying set of basis functions. Ideally these functions decay exponentially fast in space. Side profiles of the Wannier modes in Fig. 3 are shown in Fig. 4. In each case a curve is selected in order highlight the rapid decay of the Wannier modes. Numerically, all cases are found to decay exponentially fast, however the $p = 2$ mode in Fig. 4(b) is the slowest of the four. This is expected based on the spread minimization results in Appendix A 2.

With the key assumption, about how to find Wannier modes, addressed we next provide an outline of how we obtain our discrete model:

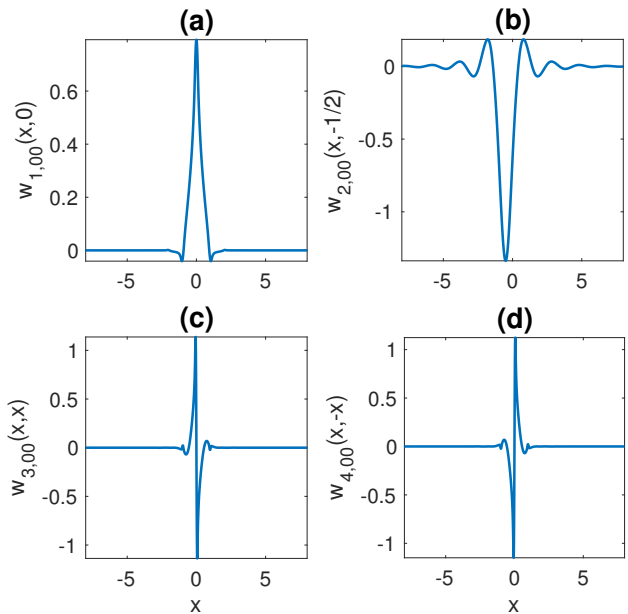


FIG. 4. Profiles of Wannier modes from Fig. 3, respectively. The Wannier modes are shown along the lines: (a) $y = 0$, (b) $y = -1/2$, (c) $y = x$, and (d) $y = -x$.

1. Numerically compute the Bloch functions (see Sec. II B).
2. Smooth Bloch functions through gradient descent optimization (see Appendix A).
3. Compute corresponding Wannier functions (see Fig. 3).
4. Use Wannier modes to calculate the coefficients of the discrete model (see Sec. IV).
5. Solve resulting tight-binding approximation: coupled system of ODEs (see Secs. V and VI).

IV. DERIVATION OF TIGHT-BINDING MODEL

We now derive our discrete tight-binding model using the Wannier functions found above as a basis. Combine the electric field given in (15)-(16) in terms of the Wannier expansion

$$E(\mathbf{r}, \mathbf{k}) = \sum_{p=1}^{\infty} \sum_{m,n=-\infty}^{\infty} \alpha_{p,mn}(\mathbf{k}) w_{p,mn}(\mathbf{r}), \quad (21)$$

where $\alpha_{p,mn}$ combines the coefficient in (15) and the phase of (16). The $w_{p,00}(\mathbf{r})$ Wannier modes are shown in Fig. 3. All other Wannier modes are obtained through integer shifts, see Eq. (18). Take expansion (21) and sub-

stitute it into the *full* ($\mathcal{M}(\mathbf{r}) \neq \mathbf{0}$) system (6) to obtain

$$\begin{aligned} \sum_p \sum_{m,n} \alpha_{p,mn} \left[-\nabla^2 w_{p,mn} + \mathcal{M}(\mathbf{r}) \cdot \nabla w_{p,mn} \right] \\ = \omega^2(\mathbf{k}) \sum_p \sum_{m,n} \alpha_{p,mn} \epsilon \tilde{\mu} w_{p,mn} . \end{aligned} \quad (22)$$

Multiplying through by $w_{\ell,m'n'}^*$ and integrating over \mathbb{R}^2 yields

$$\begin{aligned} \sum_p \sum_{m,n} \alpha_{p,mn} \left[\langle \partial_x w_{\ell,m'n'} | \partial_x w_{p,mn} \rangle_{\mathbb{R}^2} \right. \\ \left. + \langle \partial_y w_{\ell,m'n'} | \partial_y w_{p,mn} \rangle_{\mathbb{R}^2} + \langle w_{\ell,m'n'} | \mathcal{M}(\mathbf{r}) \cdot \nabla w_{p,mn} \rangle_{\mathbb{R}^2} \right] \\ = \omega^2(\mathbf{k}) \sum_p \sum_{m,n} \alpha_{p,mn} \langle w_{\ell,m'n'} | \epsilon \tilde{\mu} w_{p,mn} \rangle_{\mathbb{R}^2} , \end{aligned} \quad (23)$$

where integration-by-parts has been applied. Utilizing the Wannier orthonormality in (20), the right-hand side reduces to

$$\begin{aligned} \sum_p \sum_{m,n} \alpha_{p,mn} \left[\langle \partial_x w_{\ell,m'n'} | \partial_x w_{p,mn} \rangle_{\mathbb{R}^2} \right. \\ \left. + \langle \partial_y w_{\ell,m'n'} | \partial_y w_{p,mn} \rangle_{\mathbb{R}^2} + \langle w_{\ell,m'n'} | \mathcal{M}(\mathbf{r}) \cdot \nabla w_{p,mn} \rangle_{\mathbb{R}^2} \right] \\ = \omega^2(\mathbf{k}) \alpha_{\ell,m'n'} . \end{aligned} \quad (24)$$

For convenience let us rewrite $m = m' + \mu$ and $n = n' + \nu$, where $\mu, \nu \in \mathbb{Z}$. So the above equation becomes

$$\begin{aligned} \sum_p \sum_{\mu,\nu} \alpha_{p,m'+\mu,n'+\nu} \left[\langle \partial_x w_{\ell,m'n'} | \partial_x w_{p,m'+\mu,n'+\nu} \rangle_{\mathbb{R}^2} \right. \\ \left. + \langle \partial_y w_{\ell,m'n'} | \partial_y w_{p,m'+\mu,n'+\nu} \rangle_{\mathbb{R}^2} \right. \\ \left. + \langle w_{\ell,m'n'} | \mathcal{M}(\mathbf{r}) \cdot \nabla w_{p,m'+\mu,n'+\nu} \rangle_{\mathbb{R}^2} \right] \\ = \omega^2(\mathbf{k}) \alpha_{\ell,m'n'} . \end{aligned} \quad (25)$$

Now define the coefficients in terms of the Laplacian and magnetic terms, respectively, of

$$\mathbb{L}_{\mu\nu}^{\ell p} \equiv \langle \partial_x w_{\ell,00} | \partial_x w_{p,\mu\nu} \rangle_{\mathbb{R}^2} + \langle \partial_y w_{\ell,00} | \partial_y w_{p,\mu\nu} \rangle_{\mathbb{R}^2} , \quad (26)$$

$$\mathbb{M}_{\mu\nu}^{\ell p} \equiv \langle w_{\ell,00} | \mathcal{M}(\mathbf{r}) \cdot \nabla w_{p,\mu\nu} \rangle_{\mathbb{R}^2} . \quad (27)$$

Note that all Wannier modes, for a given band, are merely translations of the $(m, n) = (0, 0)$ Wannier mode. The equations in (25) are now rewritten as

$$\sum_{p=1}^{\infty} \sum_{\mu,\nu=-\infty}^{\infty} [\mathbb{L}_{\mu\nu}^{\ell p} + \mathbb{M}_{\mu\nu}^{\ell p}] \alpha_{p,m+\mu,n+\nu} = \omega^2(\mathbf{k}) \alpha_{\ell,mn} , \quad (28)$$

where, for convenience, the primed index notation has been discontinued. Equation (28) is an algebraic eigenvalue problem for ω^2 as a function of \mathbf{k} ; later when we need to understand dynamics, this system is transformed to differential equations by replacing ω with $-i\partial_t$.

The lattice sites of the tight-binding model consist of two interpenetrating square lattices: integer ($p = 1, 3, 4$) and half-integer ($p = 2$), centered, respectively, at the points

$$\begin{aligned} W_i &\equiv \{ (x_m, y_n) | x_m = m, y_n = n \} , \\ W_h &\equiv \{ (x_m, y_n) | x_m = m - 1/2, y_n = n - 1/2 \} , \end{aligned} \quad (29)$$

where $m, n \in \mathbb{Z}$. This means the (m, n) Wannier mode for $p = 1, 3, 4$ [$p = 2$] is centered at the spatial location (m, n) [$(m - 1/2, n - 1/2)$]. Since the algorithm in [24] mixes modes $p = 2, 3, 4$ we cannot ascribe significance to any one of these modes. As discussed above, the Wannier functions in Fig. 3 are exponentially decaying functions. As such, the coefficients in (26) and (27) are negligibly small for $\sqrt{\mu^2 + \nu^2} \gg 1$. The infinite series in (28) can be truncated to a tractable number of interactions by neglecting long-range interactions. This is the tight-binding approximation.

For the results in Secs. V and VI we consider all neighboring sites that are distance of one or less away from a central lattice site. This amounts to a total of 17 ($p = 2$) or 19 ($p = 1, 3, 4$) interactions to consider and has been demonstrated to give reasonable results for a manageable number of interactions. As the number of interactions increases the accuracy of the band diagrams tends to improve. In Appendix C we present a few band diagrams that have additional interactions and see how they compare.

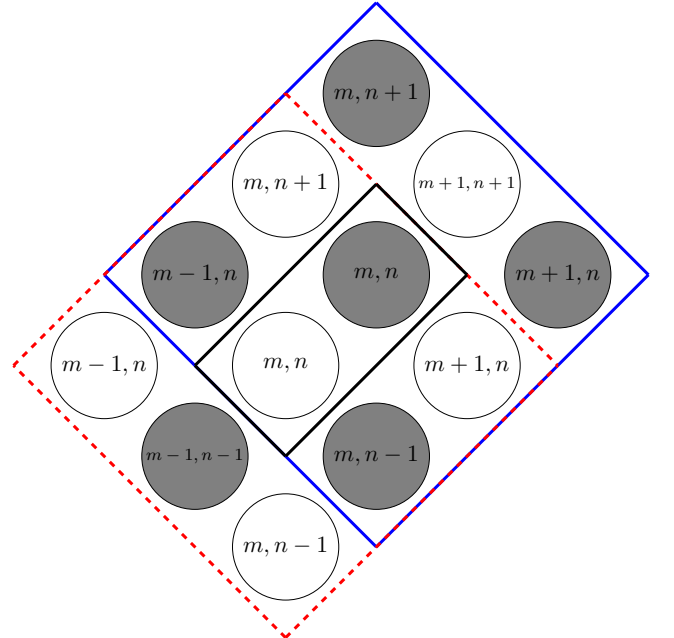


FIG. 5. (color online) Wannier mode locations and tight-binding interactions. Gray circles indicate the location of the $p = 1, 3, 4$ Wannier modes (integer sites). White circles are where the $p = 2$ modes are centered (half-integer sites). For the gray (white) circle in the center black box, the solid blue (dashed red) box encloses all Wannier interactions of distance one or less away.

A diagram organizing the interactions that are taken into account in the tight-binding approximation is displayed in Fig. 5. The circles correspond to locations of the Wannier modes given in (29): white circles at half-integer sites and gray circles at integer sites. Recall the $p = 2$ mode is centered at (white) half-integer sites [see Fig. 3(b)], while the $p = 1, 3, 4$ modes are centered at (gray) integer sites [see Figs. 3(a,c-d)]. Define \mathbf{d}_s to be the set of all lattice sites that are euclidean distance s or less away. The $s = 1$ case is shown in Fig. 5. For the central white (gray) lattice site in the black box, the red (blue) box indicates all Wannier mode locations that are distance s or less away. These are the Wannier modes whose interactions will be considered. All other interactions with Wannier modes outside \mathbf{d}_s are neglected.

For example, in the \mathbf{d}_1 case modes centered at the central white (gray) circle interact with itself and modes located at the four nearest gray (white) circles, which are a distance of $1/\sqrt{2}$ away. Additionally, the central white (gray) site interacts with the four next-nearest white (gray) circles, distance 1 away.

The infinite system in (28) is truncated to the four lowest spectral bands and rewritten as

$$\sum_{p=1}^4 \sum_{\mu, \nu \in \mathbf{d}_s} [\mathbb{L}_{\mu\nu}^{\ell p} + \mathbb{M}_{\mu\nu}^{\ell p}] \alpha_{p, m+\mu, n+\nu} = \omega^2(\mathbf{k}) \alpha_{\ell, mn} , \quad (30)$$

for $\ell = 1, 2, 3, 4$. Taking the inverse Fourier transform of this equation is equivalent to replacing ω with $-i\partial_t$. Hence the time-dependent coupled mode equations are given by

$$\frac{d^2 a_{\ell, mn}}{dt^2} + \sum_{p=1}^4 \sum_{\mu, \nu \in \mathbf{d}_s} [\mathbb{L}_{\mu\nu}^{\ell p} + \mathbb{M}_{\mu\nu}^{\ell p}] a_{p, m+\mu, n+\nu} = 0 , \quad (31)$$

where $\ell = 1, 2, 3, 4$ and $a_{p, mn}(t) = \alpha_{p, mn} \exp(i\omega t)$. The updated (time-dependent) electric field is given by

$$\bar{\mathbf{E}}(\mathbf{r}, \mathbf{k}, t) = \sum_p \sum_{m, n} a_{p, mn}(\mathbf{k}, t) w_{p, mn}(\mathbf{r}) . \quad (32)$$

Adding the complex conjugate to this function gives the (real) field defined in (1), i.e. $\mathbf{E}(\mathbf{r}, t) = (0, 0, \bar{\mathbf{E}}(\mathbf{r}, t)) + (0, 0, \bar{\mathbf{E}}^*(\mathbf{r}, t))$. The function in (32) is effectively the inverse Fourier transform of the expansion in (21).

It is from Eqs. (30) and (31) we derive our discrete results which are discussed below. In Sec. V we compute the bulk and edge bands directly from (30). The bands illuminate the relationship between the presence of topological invariants and the corresponding number and nature of gapless edge states. Then in Sec. VI we solve the initial boundary value problem in (31) and observe the unidirectional propagation of a topologically protected mode.

V. SPECTRAL BANDS: DISCRETE MODEL

In this section we compute discrete approximations of the spectral bands for the bulk (infinite) and edge (semi-

infinite) problems. For the bulk problem we can compare directly with the spectral bands found in Sec. II B. From our discrete approximation of the bands we establish the presence of nontrivial Chern numbers in the model. Nonzero Chern numbers indicates the presence of topologically protected gap modes when an edge is introduced, via the bulk-edge correspondence [21]. Next, in the edge problem we consider a semi-infinite strip domain with Dirichlet zero boundary conditions along the top and bottom sides. Beyond these boundaries (outside the lattice region) the electric field is assumed to be negligibly small. Perpendicular to these walls we look for localized eigenmodes called *edge modes*. Topologically protected modes manifest themselves as a family of localized eigenmodes whose corresponding eigenvalues span the gap between two bulk bands.

To obtain the coefficients used in this paper, a basic simulation that ran on a standard desktop computer was used. Most of that time was spent on computing the Bloch modes in (13) and the discrete model coefficients in (26) and (27). This is a one-time overhead cost. With these in hand, the discrete system in this section can be solved on a laptop computer.

A. Discrete Approximation of Bulk Bands

To approximate the spectral dispersion surfaces found in Sec. II B we look for plane wave solutions of the form $\alpha_{p, mn}(\mathbf{k}) = \alpha_p(\mathbf{k}) e^{i\mathbf{k} \cdot \mathbf{R}_{mn}}$ in Eq. (30). The governing coupled-mode system is

$$\sum_{p=1}^4 \sum_{\mu, \nu \in \mathbf{d}_s} [\mathbb{L}_{\mu\nu}^{\ell p} + \mathbb{M}_{\mu\nu}^{\ell p}] \alpha_p e^{i\mathbf{k} \cdot \mathbf{R}_{\mu\nu}} = \omega^2(\mathbf{k}) \alpha_{\ell}(\mathbf{k}) , \quad (33)$$

for $\ell = 1, 2, 3, 4$. This system can be rewritten as the 4×4 eigenvalue problem

$$\mathbb{N}(\mathbf{k}) \mathbf{a} = \omega^2(\mathbf{k}) \mathbf{a} , \quad \mathbf{a}(\mathbf{k}) = (\alpha_1, \alpha_2, \alpha_3, \alpha_4)^T , \quad (34)$$

with matrix elements

$$[\mathbb{N}_{\ell p}(\mathbf{k})] = \sum_{\mu, \nu \in \mathbf{d}_s} [\mathbb{L}_{\mu\nu}^{\ell p} + \mathbb{M}_{\mu\nu}^{\ell p}] e^{i\mathbf{k} \cdot \mathbf{R}_{\mu\nu}} .$$

Eigenvalues/eigenfunctions for (34) are computed for values of \mathbf{k} along the perimeter of the irreducible Brillouin zone [see Fig. 1(c)]. In all examples considered below we take $s = 1$ i.e. interactions between nearest and next-nearest neighbor (see Fig. 5). In Fig. 6 the discrete approximations (circles) are plotted on top of the numerically generated bands (solid curves), originally shown in Figs. 2(b) and 2(c). In all cases we only show the real part of ω , as the imaginary part is typically quite small. First, consider when $\mathcal{M}(\mathbf{r}) = \mathbf{0}$ (equivalently $\mathbb{M}_{\mu\nu}^{\ell p} = 0$). The top three bands of Fig. 6(a) form a disjoint subset of entangled bands that touch at the $\Gamma(0, 0)$ and $M(\pi, \pi)$ points.

Now we turn our attention to the $\mathcal{M}(\mathbf{r}) \neq \mathbf{0}$ (equivalently $\mathbb{M}_{\mu\nu}^{\ell p} \neq 0$) case. Physically, this corresponds to the

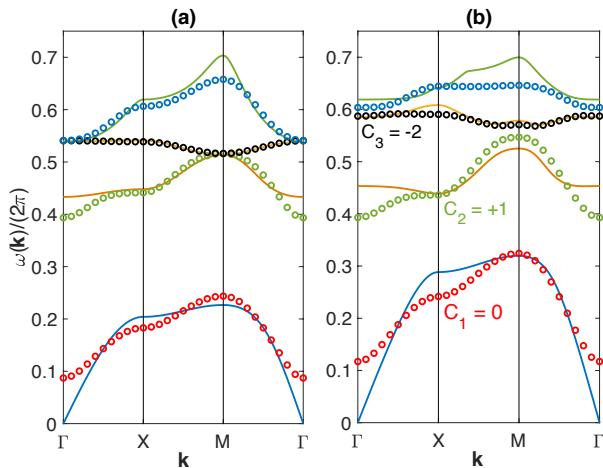


FIG. 6. Comparison between discrete spectral bands and the numerical bands shown in Figs. 2(b-c). (a) $M_{\mu\nu}^{\ell p} = 0$ ($\mathcal{M}(\mathbf{r}) = \mathbf{0}$) and (b) $M_{\mu\nu}^{\ell p} \neq 0$ ($\mathcal{M}(\mathbf{r}) \neq \mathbf{0}$). The numerical bands are denoted by solid curves and the discrete by circles. Included are the Chern numbers, defined in (14), computed from the discrete model.

introduction of an external magnetic field and breaking of time-reversal symmetry. Overall the discrete bands shown in Fig. 6(b) serve as good approximations to the numerics. Among the upper three bands the relative error is 11.5% or less across the entire Brillouin zone. Moreover these bulk bands also preserve the inversion symmetry of the lattice i.e. $\omega(\mathbf{k}) = \omega(-\mathbf{k})$. A quantitative comparison between the bands is summarized in Table II of Appendix C for different values of s .

We note a weak instability in $\mathcal{M}(\mathbf{r}) \neq \mathbf{0}$ case for some of the frequencies, with $\Im\omega(\mathbf{k})$ on the order of 0.01 or less. We attribute this spurious instability to the perturbation approximation underlying our approach. In spite of this we point out that the edge modes shown in the next section are quite stable, the unstable modes appear to only occur in bulk modes. As long as we do not excite any unstable frequencies, we had no problem computing over long times. Finally, we point out that there is no instability in the $\mathcal{M}(\mathbf{r}) = \mathbf{0}$ case.

Inspection of the discrete bands in Fig. 6(b) reveals the formation of two gaps: one between the second and third bands and another between the third and fourth bands. There is a full gap between the second and third bands throughout the entire Brillouin zone, which we refer to as a *zone gap*. There is also small zone gap that exists between the third and fourth bands. The frequency gaps are in the ranges (0.547, 0.568) and (0.592, 0.604), respectively.

As indicated above, breaking time-reversal symmetry is associated with nontrivial Chern numbers in the spectral bands [4, 5]. The Chern number is a time-independent topological invariant that is robust against lattice defects and deformations along the boundary. Moreover, through the bulk-edge correspondence, a nonzero Chern number indicates the presence of a topologically protected edge state [21]. The 2D Chern number

of the p^{th} spectral band is defined by (14) where

$$\mathbf{A}_p(\mathbf{k}) = \langle \mathbf{a}_p | \partial_{k_x} \mathbf{a}_p \rangle \hat{\mathbf{x}} + \langle \mathbf{a}_p | \partial_{k_y} \mathbf{a}_p \rangle \hat{\mathbf{y}}, \quad (35)$$

is the Berry connection given in terms of the eigenmodes of (34). The vector \mathbf{a}_p is an eigenvector of the matrix (34) corresponding to the p^{th} eigenvalue, sorted in ascending order. Here we take the complex inner-product $\langle \mathbf{f}(\mathbf{k}) | \mathbf{g}(\mathbf{k}) \rangle \equiv \mathbf{f}(\mathbf{k})^\dagger \mathbf{g}(\mathbf{k})$ for the vectors \mathbf{f} and \mathbf{g} . The Chern numbers are computed using the algorithm given in [23]. The second and third bands in Fig. 6(c) are found to possess nontrivial Chern numbers. The Chern values for the first three bands agree with those found in the continuous problem, shown in Fig. 2(c). In the next section we show that the number and chirality of edge states is consistent with these Chern numbers.

B. Discrete Edge Bands

We now look for eigenmodes in the edge problem. This problem is formulated as the solution of (30) on a strip domain that is infinite in the $x(m)$ -direction and finite with Dirichlet zero boundary conditions in the $y(n)$ -direction. Localized along both the top and bottom walls we identify edge modes whose corresponding eigenvalues lie in the band gaps. Edge modes are eigenmodes characterized by exponential decay away from the boundary wall. Furthermore, we can relate the quantity and chirality of these edge states to the Chern numbers found above.

Let us consider modes of the form $a_{p,mn}(t) = a_{p,n}(k_x) e^{i(mk_x + \omega t)}$ in Eq. (31). Then the governing systems of equations is

$$\sum_{p=1}^4 \sum_{\mu, \nu \in \mathbf{d}_s} [\mathbb{L}_{\mu\nu}^{\ell p} + M_{\mu\nu}^{\ell p}] a_{p,n+\nu} e^{i\mu k_x} = \omega^2(k_x) a_{\ell,n}, \quad (36)$$

for $\ell = 1, 2, 3, 4$. This eigenvalue problem for ω^2 is solved for values of k_x in the interval $[-\pi, \pi]$.

Now let us incorporate the top and bottom wall boundary conditions. An edge mode consists of a sharp termination at a boundary wall with exponential decay perpendicular to the wall, which can be imposed by Dirichlet zero conditions. As a result of the integer and half-integer sites, there are at least two different ways to set the edge. Here we concentrate on boundary walls whose top and bottom rows consist of integer lattice sites i.e. of ferrite rods. Recall these are the locations of the $p = 1, 3, 4$ Wannier modes. This means we create a sharp termination of the problem immediately after the first or last integer lattice site rows (see Fig. 14(a) for an illustration). The Dirichlet zero boundary conditions we impose on Eq. (36) are

$$\begin{aligned} p = 1, 3, 4 : & \quad a_{p,n} = 0, \quad \text{for } |n| > N, \\ p = 2 : & \quad a_{p,n} = 0, \quad \text{for } n \leq -N \text{ and } n > N. \end{aligned} \quad (37)$$

Notice there is one less row of half-integer lattice sites. The edge bands for half-integer boundary conditions are

discussed in Appendix B. Changing the boundary condition is found to affect the edge state eigenmode curves, but not the bulk bands.

The result of solving (36) with (37) for interactions of distance one or less is shown in Fig. 7. In both figures the solid black regions correspond to non-localized bulk modes, while the highlighted curves are gapless bands whose corresponding eigenmodes are localized near the edges. First, in Fig. 7(a) we show the dispersion bands that result when $\mathcal{M}(\mathbf{r}) = \mathbf{0}$. Here we see only bulk bands and no edge modes. Next, in Fig. 7(b) we set $\mathcal{M}(\mathbf{r}) \neq \mathbf{0}$ and see the opening of new band gaps is accompanied by a family of curves that span these gaps.

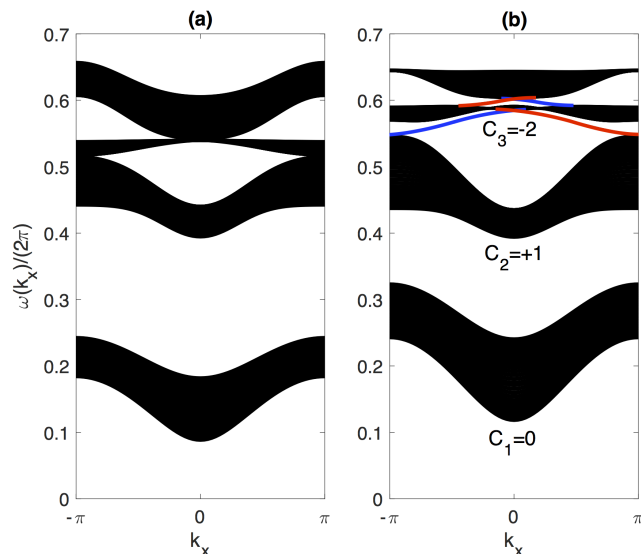


FIG. 7. The $p = 1, 2, 3, 4$ dispersion bands (ascending order) found by solving edge problem (36) with (37) for (a) $\mathbb{M}_{\mu\nu}^{\ell p} = 0$ and (b) $\mathbb{M}_{\mu\nu}^{\ell p} \neq 0$.

Next focus on the gapless edge bands that lie in-between the second, third and fourth bands. A closer view of the bands from Fig. 7(b) is shown in Fig. 8(a). Each gap has a pair of edge modes, one on the top boundary (red curve) and one on the bottom boundary (blue curve), that constitute a single chiral state. The modes spanning the gap between the second and third bands have a clockwise orientation (as viewed from the positive z direction) since a wide envelope along the bottom (top) edge will have negative (positive) group velocity. Note that we have taken solutions of the form $\exp(i(mk_x + \omega t))$, so the group velocity moves in the $\text{sgn}(-\omega'(k_x))$ direction. Two representative edge states are displayed in Figs. 8(d) and 8(e) corresponding to the bottom and top walls, respectively. In the eigenmodes we see that the (half-integer site) $p = 2$ mode has a much smaller magnitude than the (integer site) $p = 3, 4$ modes. This says that the electric field has a higher intensity close to the YIG rods.

We also notice that the $p = 1$ part of the eigenmodes we find are effectively zero for large ω corresponding to the upper three bands, and vice versa for eigenfrequen-

cies in the first bulk band. There is an apparent decoupling between the first mode and the second through fourth modes. This suggests that the system (36) could be decoupled into two parts: $p = 1$ and $p = 2, 3, 4$ and solved separately. We have implemented this decoupling and noticed that it did not significantly affect any of the band diagrams.

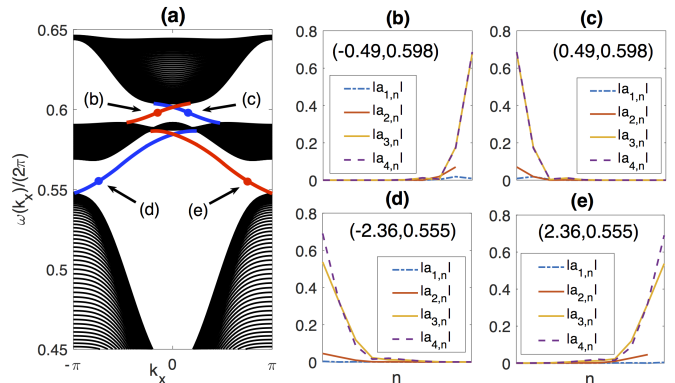


FIG. 8. (color online) (a) A closer view of the band gaps in Fig. 7(b). A red (blue) curve denotes a family of edge modes localized along the top (bottom) edge. The magnitude of the eigenmodes at the point $(k_x, \omega/(2\pi))$ are shown in panels (b-e).

Moving up to the band gap between the third and fourth bands the orientation an envelope will move is counter-clockwise. We point that this is in the *opposite* direction from what was found in the lower gap and will consequently have an *opposite* chirality sign [19]. Overall the width of this zone gap is rather small, but we are still able to identify frequencies that support edge states totally in the gap region. Representative edge states are shown in Fig. 8(b) and 8(c) localized along the top and bottom edges, respectively. Again, near the edge the half-integer eigenmode is found to be small in comparison to the $p = 3, 4$ modes, meanwhile the $p = 1$ mode is even smaller.

There is a direct connection between the bulk Chern numbers and the chirality and number of edge modes. Define the clockwise direction, when viewed from above, as the positive direction. Let us denote the band gap between the first and second bulk bands as the $p = 1$ (first) gap, and from there the gap index increases with ω i.e. $p = 2, 3, \dots$ (second, third, ... gaps). The bulk-edge correspondence gives the relationship

$$\mathcal{I}_p = \sum_{q=1}^p C_q, \quad (38)$$

where \mathcal{I}_p is the gap Chern number i.e. the number of gapless modes (taking into account the orientation) of the p^{th} band gap and C_q is the Chern number corresponding to the q^{th} bulk band. This quantity gives the sum of the (signed) topologically protected modes within that gap. We point out that \mathcal{I}_p is equivalent (up to multiplicative constant) to the Hall conductance considered

p	C_p	\mathcal{I}_p	\mathcal{N}_p	\mathcal{P}_p
1	0	0	0	0
2	1	1	0	1
3	-2	-1	1	0

TABLE I. Bulk-edge correspondence between bulk and gap Chern numbers.

in the quantum Hall effect [10]. This sum can also be expressed as $\mathcal{I}_p \equiv \mathcal{P}_p - \mathcal{N}_p$, where \mathcal{P}_p (\mathcal{N}_p) is the number of positive (negative) chiral modes in the p^{th} gap. We note that from the gap Chern number alone we are unable to uniquely determine the number of gap edge modes, namely \mathcal{P}_p and \mathcal{N}_p .

The topological values for this system are organized in Table I. Using the Chern numbers shown in Fig. 7(b) we calculate the gap Chern number (38) for the first three band gaps. Through examination of the edge bands in Fig. 8(a) we are able to verify that the second band gap contains one positive mode and the third gap has one negative chiral mode. An equivalent way of establishing the bulk-edge correspondence is through the difference $C_p = \mathcal{I}_p - \mathcal{I}_{p-1}$. If we take $\mathcal{I}_0 \equiv 0$, then this definition is also consistent with the edge band diagram.

VI. TIME EVOLUTION

In this section we consider dynamics via time evolution of the tight-binding model. We consider two distinct initial boundary value problems. First, we integrate the system for a wide envelope initial condition. The envelope is observed to move unidirectionally with group velocity and propagate without backscatter through lattice defects. Later we look at the dynamics due to introducing a delta function source modeling an input antenna. We find that the source also excites unidirectional flow localized along the edge.

The system of interest is that of the coupled mode system in (31). For simplicity the domain is taken to be rectangular. The boundary conditions will consist of integer lattice sites, similar to that shown in Fig. 14(a), in both directions. Specifically we impose the following boundary conditions:

$$\begin{aligned}
 p = 2 : \quad & a_{p,mn} = 0 & (39) \\
 \text{for } n \leq -N, n > N, \text{ and } m \leq -M, m > M, \\
 p = 1, 3, 4 : \quad & a_{p,mn} = 0 \\
 \text{for } |n| > N, \text{ and } |m| > M,
 \end{aligned}$$

where M, N are large integers. For the computational results shown in Figs. 9, 10, 11, and 12 we take $N = 25$ and $M = 125$ for the envelope or $M = 75$ for the source. The system of ODEs is integrated using a fourth order Runge-Kutta method.

To initialize the envelope function we take

$$a_{p,mn}(0) = \text{sech}[\nu(m - m_0)] a_{p,n}(k_x, \omega) e^{imk_x}, \quad (40)$$

for $p = 1, 2, 3, 4$ for the hyperbolic secant centered at $m = m_0$. The wavenumber k_x and numerically computed eigenmode $a_{p,n}(k_x, \omega)$ correspond to an eigenvalue that resides in the gap located between the second and third bulk bands in Fig. 8(a). In particular, we take the frequency that corresponds to the edge mode shown in Fig. 8(e). The width parameter ν is taken to be small so that only gap modes are excited.

In order to probe the robustness of this mode, we propagate it into a defect and monitor the scattering. The defect we wish to model is a region adjacent to the wall through which the electric field can not propagate, and so it must go around or scatter. This boundary condition is effectively a large potential barrier wall through which the field can not penetrate. To approximate this scenario we set the field coefficients to be zero at the lattice sites in this region.

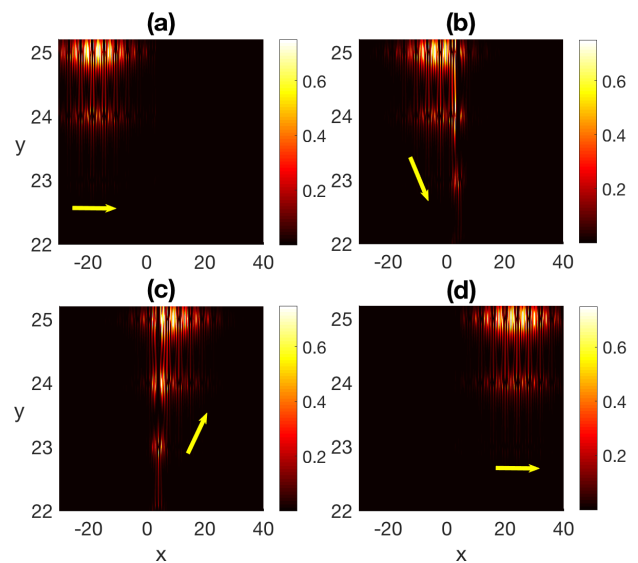


FIG. 9. Envelope evolution impacting a defect for initial condition (40) with $\nu = 0.125, m_0 = -25$ and $(k_x, \omega/(2\pi)) = (2.36, 0.555)$. Shown is the intensity of electric field at (a) $t = 100$, (b) $t = 300$, (c) $t = 480$, and (d) $t = 700$. A lattice defect is imposed at lattice integer sites $p = 1, 3, 4, m = 4, 24 \leq n \leq 25$ and at half-integer sites $p = 2, 4 \leq m \leq 5, 24 \leq n \leq 25$.

The evolution of the envelope into an edge defect is presented in Figs. 9 and 10 which show the the intensity of the electric field and intensity of the modal envelope, respectively. The electric field in Fig. 9 corresponds to the (real-valued) field in (1). To find the electric field of the TM equation we use the expansion defined in (32). Shown in Fig. 10 is the $a_{4,mn}$ mode since it is one of the dominant modes [see Fig. 8(e)] and it helps visualize the location of the envelope. Before encountering the defect the envelope is found to propagate with group velocity $-\omega'(k_x) \approx 0.0781$ of the edge bands in Fig. 8(a). Upon collision with the defect the envelope does *not* backscatter. Instead it maneuvers around the defect and exits with almost no loss of intensity and the same form it entered with. From this simulation we see that the energy of this system moves (with group velocity) in only one

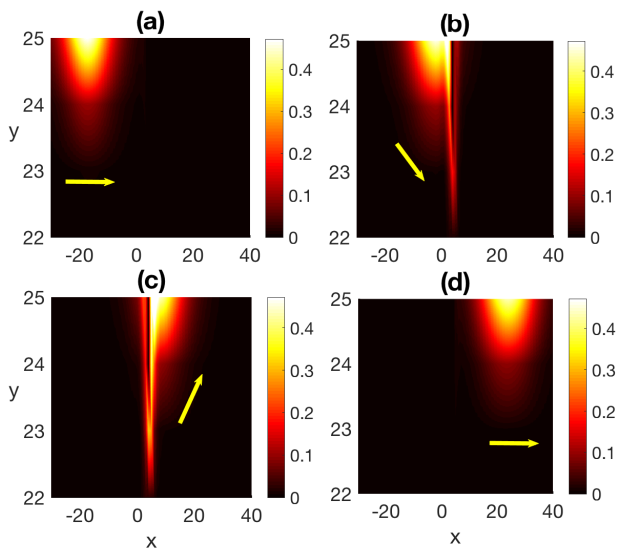


FIG. 10. Envelope evolution impacting a defect for initial condition (40) with $\nu = 0.125$, $m_0 = -25$ and $(k_x, \omega/(2\pi)) = (2.36, 0.555)$. Intensity of $a_{4,mn}$ mode at (a) $t = 100$, (b) $t = 300$, (c) $t = 480$, and (d) $t = 700$. A lattice defect is imposed at lattice integer sites $p = 1, 3, 4$, $m = 4$, $24 \leq n \leq 25$ and at half-integer sites $p = 2, 4$, $4 \leq m \leq 5$, $24 \leq n \leq 25$.

direction. More importantly, without topological protection an envelope mode like this would not possess the robust unidirectionality seen in Figs. 9-10.

Next we consider an initially zero field that is excited by a source. To incorporate the source term we modify Eq. (31) to

$$\frac{d^2 a_{\ell,mn}}{dt^2} + \sum_{p=1}^4 \sum_{\mu, \nu \in \mathbf{d}_s} [\mathbb{L}_{\mu\nu}^{\ell p} + \mathbb{M}_{\mu\nu}^{\ell p}] a_{p,m+\mu,n+\nu} = \frac{dJ_{\ell,mn}}{dt}, \quad (41)$$

where $\ell = 1, 2, 3, 4$ and $J_{\ell,mn}(t) = C_{\ell} \delta_{mq} \delta_{nr} \tanh(bt) e^{i\omega t}$ is a time-harmonic source at large times. The point (q, r) indicates the location of the source (near the top edge), while C_{ℓ} allows us to control which modes we excite, and the hyperbolic tangent function is included to gradually ramp the source up from zero. For the simulation below we look to place an antenna in the region where there is no lattice rods i.e. at a half-integer lattice site. For this reason we take $C_{\ell} = \delta_{\ell 2}$. The source is placed at $(q, r) = (0, 25)$ (close to the edge) so that it will excite an edge mode. In terms of continuous variables, the spatial location of the source corresponds to the point $(x, y) = (-0.5, 24.5)$. As an initial condition we take $a_{\ell,mn}(t = 0) = 0$.

The evolution of the defect-free problem is summarized in Fig. 11. Starting from zero, the source (at a band gap frequency) slowly ramps up to full strength and begins to excite an edge mode. Instead of propagating in all directions the edge state only flows from left to right, unidirectionally. The edge mode slowly begins to fill the wall with a wave front that travels approximately with the group velocity. After this early transient period, the system appears to transition into a steady-state with the

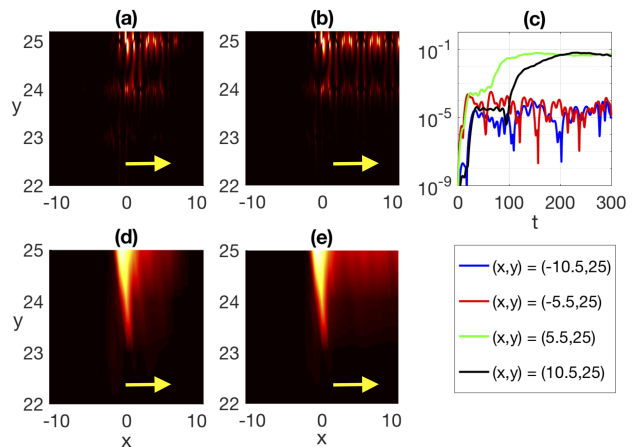


FIG. 11. (color online) Evolution of the electric field at frequency $(k_x, \omega/(2\pi)) = (2.36, 0.555)$. Snapshots of the intensity at time (a) $t = 100$ and (b) $t = 300$. (c) Time evolution of the electric field intensity at points to the left and right of the source. Intensity of $a_{4,mn}$ mode at (d) $t = 100$ and (e) $t = 300$.

electric field concentrated near the top most lattice rods. To highlight the unidirectional flow of the wave we measure the field intensity at points to the left and right of the source. As shown in Fig. 11(c), the difference between the intensity to the right and left of the source is three to four orders of magnitude. Also included in Figs. 11(d) and 11(e) is the modal coefficient $a_{4,mn}(t)$ used to compute Figs. 11(a) and 11(b), respectively.

Next we examine the evolution of a source induced edge mode when it encounters a lattice defect. Using the same initial condition as before, the source slowly excites the unidirectional edge state shown in Fig. 12. When the mode encounters the lattice defect it does not backscatter at all. Instead it flows around the defect and eventually rejoins the original wall. The flow of the field can be seen in Fig. 12(c) where leftward flow is negligibly small in comparison to the right direction. The robust unidirectional motion seen here is similar to that seen in Figs. 9-10; and is attributed to topology; i.e. the presence of a nonzero gap Chern number.

VII. CONCLUSIONS

This paper presents the first complete tight-binding model for the TM Maxwell equation with an external magnetic field that can be used to effectively describe the underlying wave dynamics and associated topological effects. This discrete model accurately describes the results in [7]. The method relies on expansion in terms of suitable Wannier functions. To find these Wannier functions the algorithm in [24] was useful. Applying the external magnetic field introduces an anisotropic gyrotropic response in the permeability which breaks time-reversal symmetry. These magnetic effects induce non-

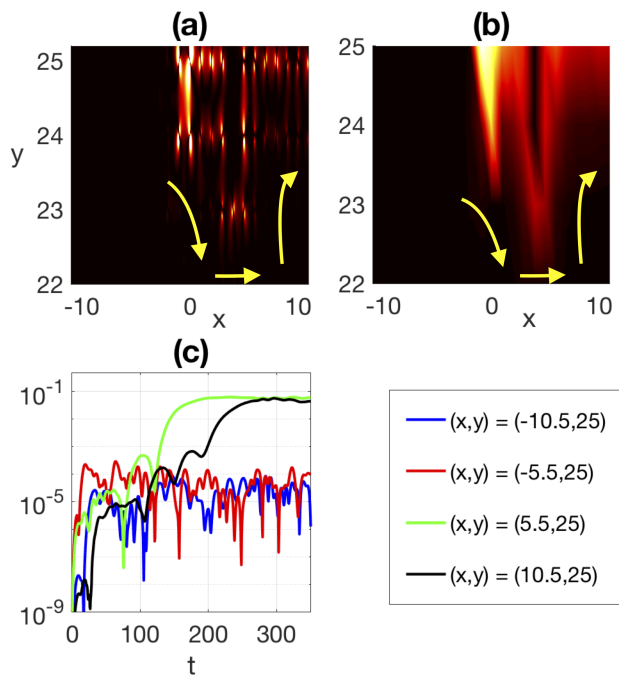


FIG. 12. (color online) Evolution of the electric field at frequency $(k_x, \omega/(2\pi)) = (2.36, 0.555)$ in the presence of a defect. A lattice defect is imposed at lattice integer sites $p = 1, 3, 4, m = 4, 24 \leq n \leq 25$ and at half-integer sites $p = 2, 4 \leq m \leq 5, 24 \leq n \leq 25$. (a) Snapshot of the electric field intensity at time $t = 350$. (b) Snapshot of the modal intensity of $a_{4,mn}$ at $t = 350$. (c) Time evolution of the electric field intensity at points to the left and right of the source.

trivial topology which in turn prevents a direct expansion in terms of Wannier modes. Instead a perturbative approach was used to obtain a set of Wannier modes from the closely related (time-symmetric) problem in order to model the full problem which does not have time-reversal symmetry.

With these Wannier modes a set of tight-binding equations were derived that yield accurate approximations of the actual spectral bands. Importantly, this discrete system produces band approximations with nontrivial Chern numbers and topologically protected edge modes. The Chern numbers/edge modes agree with the bulk-edge correspondence. The edge modes whose frequencies lie in the band gap were found to propagate unidirectionally, without backscatter around lattice defects.

This tight-binding model provides qualitative agreement with full numerical simulations at a fraction of the cost. Solutions of the discrete model can be performed on a small laptop in a relatively short amount of time. This approach serves as an alternative to direct numerics and paves the way for developing coupled mode models in other problems with nontrivial Chern numbers.

VIII. ACKNOWLEDGEMENT

This work was partially supported by AFOSR under grant No. FA9550-19-1-0084.

-
- [1] T. Ozawa, H. M. Price, A. Amo, N. Goldman, M. Hafezi, L. Lu, M. C. Rechtsman, D. Schuster, J. Simon, O. Zilberberg, and I. Carusotto, *Rev. Mod. Phys.* **91** 015006, (2019).
- [2] M. A. Bandres, S. Wittek, G. Harari, M. Parto, J. Ren, M. Segev, D. N. Christodoulides, M. Khajavikhan, *Science* **359** eaar4005, (2018).
- [3] B. Bahari, A. Ndao, F. Vallini, A. El Amili, Y. Fainman, B. Kanté Science **358** pp. 636, (2017).
- [4] F.D.M. Haldane and S. Raghu, *Phys. Rev. Lett.*, **100** 013904, (2008).
- [5] S. Raghu and F.D.M. Haldane, *Phys. Rev. A*, **78** 033834, (2008).
- [6] J. P. Lee-Thorp, M. I. Weinstein, and Y. Zhu, *Arch Rational Mech Anal.*, **232** pp. 1, (2019).
- [7] Z. Wang, Y.D. Chong, J. D. Joannopoulos, and M. Soljačić, *Phys. Rev. Lett.*, **100** 013905, (2008).
- [8] D. M. Pozar, *Microwave Engineering*, John Wiley & Sons, Inc., (2011).
- [9] K. v. Klitzing, G. Dorda, and M. Pepper, *Phys. Rev. Lett.*, **45** pp. 494, (1980).
- [10] D. J. Thouless, M. Kohmoto, M. P. Nightingale, and M. den Nijs, *Phys. Rev. Lett.*, **49** pp. 405, (1982).
- [11] Z. Wang, Y.D. Chong, J. D. Joannopoulos, and M. Soljačić, *Nature*, **461** pp. 772, (2009).
- [12] X. Ao, Z. Lin, and C. T. Chan, *Phys. Rev. B*, **80** 033105, (2009).
- [13] Y. Poo, R.-X. Wu, Z. Lin, Y. Yang, and C. T. Chan, *Phys. Rev. Lett.*, **106** 093903, (2011).
- [14] M.C. Rechtsman, J.M. Zeuner, Y. Plotnik, Y. Lumer, D. Podolsky, F. Dreisow, S. Nolte, M. Segev, and A. Szameit, *Nature*, **496**, pp. 196 (2013).
- [15] M. J. Ablowitz and C.W. Curtis and Y-P Ma, *Phys. Rev. A*, **90**, 023813, (2014).
- [16] J. Noh, S. Huang, D. Leykam, Y.D. Chong, K.P. Chen, and M.C. Rechtsman, *Nature Physics*, **13**, pp. 611 (2017).
- [17] J. Noh, S. Huang, K.P. Chen, and M.C. Rechtsman, *Phys. Rev. Lett.*, **120**, 063902 (2018).
- [18] M.J. Ablowitz and J.T. Cole, *Phys. Rev. A*, **96** 043868, (2017).
- [19] M.J. Ablowitz and J.T. Cole, *Phys. Rev. A*, **99** 033821, (2019).
- [20] C. Brouder, G. Panati, M. Calandra, C. Mourougane, and N. Marzari, *Phys. Rev. Lett.*, **98** 046402, (2007).
- [21] Y. Hatsugai, *Phys. Rev. Lett.*, **71** pp. 3697, (1993).
- [22] L. Lu, J. D. Joannopoulos, and M. Soljačić, *Nature Photonics*, **8** pp. 821, (2014).
- [23] T. Fukui, Y. Hatsugai, and H. Suzuki, *J. Phys. Soc. Jpn.*, **74** pp. 1674, (2005).
- [24] N. Marzari and D. Vanderbilt, *Phys. Rev. B*, **56** pp. 12847, (1997).

- [25] K. Busch, S. F. Mingaleev, A. Garcia-Martin, M. Schillinger, and D. Hermann, J. Phys.: Condens. Matter, **15** R1233, (2003).
 [26] E. I. Blount, Solid State Phys., **13** pp. 305, (1962).

Appendix A: The Marzari-Vanderbilt (MV) Algorithm

This appendix reviews some of the relevant ideas of the MV algorithm [24]. The algorithm is used to compute well-localized Wannier modes that are then used to compute the discrete coefficients in Sec. IV. The algorithm is needed because the numerically computed Bloch eigenfunctions from (13) are not sufficiently smooth functions of \mathbf{k} , which results in Wannier functions (17) with slow decay in \mathbf{r} .

First we introduce some preliminary definitions. In [26] it is shown that the first moment (center of mass) for the p^{th} Wannier mode located near the unit cell (UC): $[-1/2, 1/2] \times [-1/2, 1/2]$ is given by

$$\begin{aligned} \bar{\mathbf{r}}_p &\equiv \langle w_{p,00} | \mathbf{r} w_{p,00} \rangle_{\mathbb{R}^2, \epsilon\bar{\mu}} \\ &= \frac{1}{4\pi^2} \iint_{\text{BZ}} \langle u_p(\mathbf{r}, \mathbf{k}) | \nabla_{\mathbf{k}} u_p(\mathbf{r}, \mathbf{k}) \rangle_{\text{UC}, \epsilon\bar{\mu}} d\mathbf{k}, \end{aligned} \quad (\text{A1})$$

where the above norm is defined as

$$\|f\|_{\text{UC}, \epsilon\bar{\mu}}^2 = \iint_{\text{UC}} |f(\mathbf{r})|^2 \epsilon(\mathbf{r}) \tilde{\mu}(\mathbf{r}) d\mathbf{r}, \quad (\text{A2})$$

and the second moment of the p^{th} -band Wannier mode is

$$\begin{aligned} \langle |\mathbf{r}|^2 \rangle_p &\equiv \langle w_{p,00} | |\mathbf{r}|^2 w_{p,00} \rangle_{\mathbb{R}^2, \epsilon\bar{\mu}} \\ &= \frac{1}{4\pi^2} \iint_{\text{BZ}} \|\nabla_{\mathbf{k}} u_p(\mathbf{r}, \mathbf{k})\|_{\text{UC}, \epsilon\bar{\mu}}^2 d\mathbf{k}. \end{aligned} \quad (\text{A3})$$

Since all other Wannier modes $w_{p,mn}$ are merely translations of the Wannier mode located near the UC, it suffices to focus on optimizing the localization properties of the $w_{p,00}(\mathbf{r})$ modes. Next introduce the spread (variance) functional

$$\Omega = \sum_{p=2}^4 \Omega_p, \quad \Omega_p = \langle |\mathbf{r}|^2 \rangle_p - |\bar{\mathbf{r}}_p|^2. \quad (\text{A4})$$

The second, third, and fourth bands in Fig. 2 form an isolated subset of *entangled* bands. This means that somewhere throughout the Brillouin zone there are band degeneracies, or touching points, where $\omega_p(\mathbf{k}) = \omega_{p+1}(\mathbf{k})$. As such, we must solve for all entangled bands simultaneously, as a coupled system. The goal of the MV algorithm is to minimize (A4) by introducing a unitary transformation that smoothes the Bloch modes in \mathbf{k} -space.

Consider the linear combination of Bloch functions

$$\begin{aligned} \psi_q(\mathbf{r}, \mathbf{k}) &= \sum_{p=2}^4 [U_{pq}(\mathbf{k})] E_p(\mathbf{r}, \mathbf{k}) \\ &= \sum_{p=2}^4 [U_{pq}(\mathbf{k})] e^{i\mathbf{k}\cdot\mathbf{r}} u_p(\mathbf{r}, \mathbf{k}), \end{aligned} \quad (\text{A5})$$

where $U(\mathbf{k})$ is a 3×3 unitary matrix whose elements are given by $[U_{pq}(\mathbf{k})]$. Each of the Bloch functions used in (A5) are normalized to one with respect to the norm given in (A2). By taking a unitary transformation of the original Bloch modes all the orthogonality properties are inherited by their linear combination. The corresponding Wannier modes are defined in terms of (A5) and given by

$$w_{p,mn}(\mathbf{r}) = \frac{1}{4\pi^2} \iint_{\text{BZ}} e^{-i\mathbf{k}\cdot\mathbf{R}_{mn}} \psi_p(\mathbf{r}, \mathbf{k}) d\mathbf{k}. \quad (\text{A6})$$

This is the formula used to calculate the Wannier modes shown in Fig. 3.

Next we discuss the MV algorithm approach to numerically compute Wannier modes that minimize spread. Start by discretizing the Brillouin zone $[-\pi, \pi] \times [-\pi, \pi]$ by the mesh $\mathbf{k}_{m'n'} = (-\pi + \Delta k (m' + \frac{1}{2}), -\pi + \Delta k (n' + \frac{1}{2}))$ for $m', n' = 0, 1, 2, \dots, P-1$, where $\Delta k = 2\pi/P$. Integrals are replaced by trapezoidal quadratures

$$\frac{1}{4\pi^2} \iint_{\text{BZ}} d\mathbf{k} \rightarrow \frac{1}{4\pi^2} \sum_{\mathbf{k}} (\Delta k)^2 = \frac{1}{P^2} \sum_{\mathbf{k}},$$

where summation is over all points in the mesh. For functions with periodic boundary conditions in \mathbf{k} this quadrature is exponentially accurate. Next the derivatives in (A1) and (A3) are approximated by second-order accurate and centered finite-differences stencils. The gradient approximation is

$$\nabla_{\mathbf{k}} f(\mathbf{k}) \approx \sum_{\mathbf{b} \in \mathcal{S}} w_b \mathbf{b} [f(\mathbf{k} + \mathbf{b}) - f(\mathbf{k})],$$

over the set

$$\mathcal{S} = \left\{ \begin{pmatrix} \Delta k \\ 0 \end{pmatrix}, \begin{pmatrix} -\Delta k \\ 0 \end{pmatrix}, \begin{pmatrix} 0 \\ \Delta k \end{pmatrix}, \begin{pmatrix} 0 \\ -\Delta k \end{pmatrix} \right\}, \quad (\text{A7})$$

with $w_b = 1/(2\Delta k^2)$ for each vector. The following discrete approximations to the first and second moments given in (A1) and (A3), respectively, are derived in [24]

$$\bar{\mathbf{r}}_p \approx -\frac{1}{P^2} \sum_{\mathbf{k}, \mathbf{b}} w_b \mathbf{b} \text{Im} \log [M_{pp}(\mathbf{k}, \mathbf{b})], \quad (\text{A8})$$

and

$$\begin{aligned} \langle |\mathbf{r}|^2 \rangle_p &\approx \frac{1}{P^2} \sum_{\mathbf{k}, \mathbf{b}} w_b \left\{ -2 \text{Re} \log [M_{pp}(\mathbf{k}, \mathbf{b})] \right. \\ &\quad \left. + (\text{Im} \log [M_{pp}(\mathbf{k}, \mathbf{b})])^2 \right\}, \end{aligned} \quad (\text{A9})$$

where

$$[M_{pq}(\mathbf{k}, \mathbf{b})] = \langle u_p(\mathbf{r}, \mathbf{k}) | u_q(\mathbf{r}, \mathbf{k} + \mathbf{b}) \rangle_{\text{UC}, \epsilon\bar{\mu}} \quad (\text{A10})$$

are the elements of the matrix $M(\mathbf{k}, \mathbf{b})$. We point out that this inner-product is performed only once at the beginning of the algorithm below. Afterward updates

are applied directly to the matrix $M(\mathbf{k}, \mathbf{b})$. Since this matrix does not depend on space, the algorithm iterates quite fast. We also note that $M(\mathbf{k}, \mathbf{b})$ is periodic in \mathbf{k} .

In order to minimize spread functional (A4) a gradient descent optimization algorithm is implemented and used to update the unitary matrix in (A5). The descent gradient in [24] is found to be

$$\Delta W(\mathbf{k}) = \frac{\alpha}{w} \sum_{\mathbf{b}} w_b \left[\mathcal{A}[\tilde{R}(\mathbf{k}, \mathbf{b})] - \mathcal{S}[T(\mathbf{k}, \mathbf{b})] \right], \quad (\text{A11})$$

where $w = \sum_{\mathbf{b}} w_b$ and

$$\begin{aligned} [T_{pq}(\mathbf{k}, \mathbf{b})] &= [\tilde{R}_{pq}(\mathbf{k}, \mathbf{b})][Q_q(\mathbf{k}, \mathbf{b})], \\ [\tilde{R}_{pq}(\mathbf{k}, \mathbf{b})] &= \frac{[M_{pq}(\mathbf{k}, \mathbf{b})]}{[M_{qq}(\mathbf{k}, \mathbf{b})]}, \\ [Q_q(\mathbf{k}, \mathbf{b})] &= \text{Im} \ln[M_{qq}(\mathbf{k}, \mathbf{b})] + \mathbf{b} \cdot \bar{\mathbf{r}}_q. \end{aligned}$$

The operators $\mathcal{A}[B]$ and $\mathcal{S}[B]$ are defined by

$$\mathcal{A}[B] = \frac{B - B^\dagger}{2}, \quad \mathcal{S}[B] = \frac{B + B^\dagger}{2i},$$

where \dagger denotes the complex conjugate transpose. By construction, the matrix ΔW is anti-unitary i.e. $\Delta W^\dagger = -\Delta W$, and it preserves time-reversal symmetry, that is $\Delta W(-\mathbf{k}) = \Delta W(\mathbf{k})^*$. So, as a result, if an initial guess of the algorithm has time-reversal symmetry, then so will the output.

The value of α used in (A11) is taken to be small and positive, typically 0.1 in our simulations. The unitary matrix in (A5) is updated by

$$U^{(c+1)}(\mathbf{k}) = U^{(c)}(\mathbf{k}) \exp\left(\Delta W^{(c)}(\mathbf{k})\right), \quad (\text{A12})$$

where c denotes the iteration count, starting with the initial guess at $c = 0$. By construction, this update is also a unitary matrix since ΔW is anti-unitary. The matrix in (A10) is then updated by

$$M^{(c+1)}(\mathbf{k}, \mathbf{b}) = (U^{(c+1)}(\mathbf{k}))^\dagger M^{(0)}(\mathbf{k}, \mathbf{b}) U^{(c+1)}(\mathbf{k} + \mathbf{b}). \quad (\text{A13})$$

To obtain the Wannier modes shown in Fig. 3 we used the algorithm above with the initial guess described in the next section. A summary of the iteration method is given below.

1. Numerically compute the Bloch modes from Eq. (11).
2. Rescale the Bloch mode as shown in Eq. (A14).
3. Compute initial overlap matrix $M^{(0)}(\mathbf{k}, \mathbf{b})$ in Eq. (A10) using the rescaled Bloch modes.
4. Initialize unitary matrix $U^{(0)}(\mathbf{k})$ as an identity matrix.
5. Begin iteration loop, starting at $c = 0$:
 - (a) Compute anti-unitary matrix $\Delta W^{(c)}(\mathbf{k})$ in Eq. (A11).

- (b) Update the unitary matrix $U^{(c+1)}(\mathbf{k})$ in Eq. (A12).
- (c) Update overlap matrix $M^{(c+1)}(\mathbf{k}, \mathbf{b})$ in Eq. (A13).
- (d) Stop iteration when the difference in successive spreads $|\Omega^{(c+1)} - \Omega^{(c)}|$ in Eq. (A4) is less than a specified tolerance.

We remark that the first spectral band in the time-reversal *broken* problem [see Fig. 2(c)] is isolated and has trivial Chern number. As a result, after the renormalization procedure described below, the Bloch mode requires no minimization through the MV algorithm to achieve a well-localized Wannier state. Hence the first spectral mode is computed by itself. Only the Wannier modes corresponding to the second, third, and fourth spectral bands are optimized using the MV algorithm.

1. An Initial Bloch function through rescaling

The MV algorithm above requires a reasonable initial guess in order to converge to a well-localized mode. The numerically computed normalized Bloch mode is non-unique and has the form $\mathcal{E}(\mathbf{r}, \mathbf{k}) = C(\mathbf{k})E(\mathbf{r}, \mathbf{k})$ due to the linearity of (6). The function $E(\mathbf{r}, \mathbf{k})$ is a Bloch mode solution that is assumed to be sufficiently smooth in \mathbf{k} . The pre-factor part is typically non-smooth in \mathbf{k} and can be removed by a simple rescaling of the eigenfunction. If we divide $\mathcal{E}(\mathbf{r}, \mathbf{k})$ by the same function evaluated at some spatial point \mathbf{r}_0 where $\mathcal{E}(\mathbf{r}_0, \mathbf{k}) \neq 0$, then the pre-factor part of the numerical solution is canceled out and we get

$$\frac{\mathcal{E}(\mathbf{r}, \mathbf{k})}{\mathcal{E}(\mathbf{r}_0, \mathbf{k})} = \frac{C(\mathbf{k})E(\mathbf{r}, \mathbf{k})}{C(\mathbf{k})E(\mathbf{r}_0, \mathbf{k})} = \frac{E(\mathbf{r}, \mathbf{k})}{E(\mathbf{r}_0, \mathbf{k})}, \quad (\text{A14})$$

which is also a solution to (6). After doing this the Bloch function needs to be renormalized so that the norm of the Bloch mode (A2) is one. We find that this typically leads to a smoother initial guess. In our experience it is possible without too much searching to find an \mathbf{r}_0 value that leads to convergence mentioned below.

In addition to smoothing the electric field, this rescaling method also preserves the time-reversal symmetry of the $\mathcal{M}(\mathbf{r}) = \mathbf{0}$ problem. Notice that

$$\frac{\mathcal{E}^*(\mathbf{r}, -\mathbf{k})}{\mathcal{E}^*(\mathbf{r}_0, -\mathbf{k})} = \frac{E^*(\mathbf{r}, -\mathbf{k})}{E^*(\mathbf{r}_0, -\mathbf{k})} = \frac{E(\mathbf{r}, \mathbf{k})}{E(\mathbf{r}_0, \mathbf{k})} = \frac{\mathcal{E}(\mathbf{r}, \mathbf{k})}{\mathcal{E}(\mathbf{r}_0, \mathbf{k})}. \quad (\text{A15})$$

We have found it convenient (not necessary) to divide the first (isolated), second and fourth modes by the Bloch wave at the origin, while we divide the third band mode by some nonzero $\mathcal{E}(\mathbf{r}_0 \neq \mathbf{0}, \mathbf{k})$ value.

2. Convergence Results

In this section we apply the MV algorithm given above and discuss the convergence results. The Bloch functions

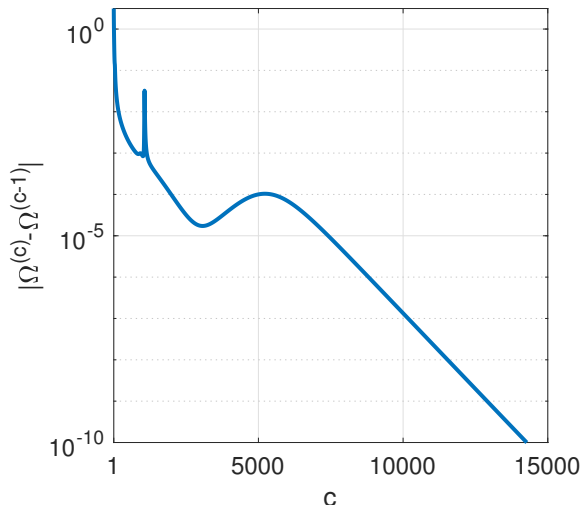


FIG. 13. Convergence of the spread functional (A4) for the three band case ($p = 2, 3, 4$).

are numerically computed using the spectral method described in Sec. II B. For these results we have discretized the Brillouin zone with a 24×24 mesh. To initialize the MV algorithm we use the rescaled initial guess in Sec. A 1. The convergence of the method is tracked by calculating the difference in successive iterations of the total spread (A4). When the difference $|\Omega^{(c)} - \Omega^{(c-1)}|$, where c is the number of iterations, is less than 10^{-10} we terminate the algorithm.

The convergence of the MV algorithm is shown in Fig. 13 as a function of the number of iterations. For the parameters and initial condition used here, the method takes 14,275 iterations to converge. The variances for the individual modes in (A4) are: $\Omega_2 = 0.3291$, $\Omega_3 = 0.0330$, and $\Omega_4 = 0.0330$. The $p = 2$ mode is observed to have the largest spread; this mode corresponds to the off-site Wannier mode shown in Fig. 3(b). The other two Wannier modes have better localization and are centered at lattice sites in Figs. 3(c-d). Finally, to obtain $p = 1$ mode we only performed the rescaling in Sec. A 1 and did not apply the MV algorithm. Doing this produced a mode with variance $\Omega_1 = 0.0445$.

Appendix B: Edge Modes with Different Boundary Conditions

This section is dedicated to showing how altering the boundary conditions can significantly change structure of the edge band diagram, while the number of edge modes remains the same. To begin, recall in Fig. 8(a) the edge bands were computed for boundaries that began and ended with integer lattice rows [see Fig. 14(a)]. However this is not the only boundary conditions we can introduce. Another option is to impose a top or bottom row that is all half-integer sites [see Figs. 14(b) and

14(c)]. Physically, we interpret this as to where the location wall boundary condition (solid black lines in Fig. 14) is placed relative to the integer or half-integer sites. Recall that the integer sites correspond to the location of ferrite rods.

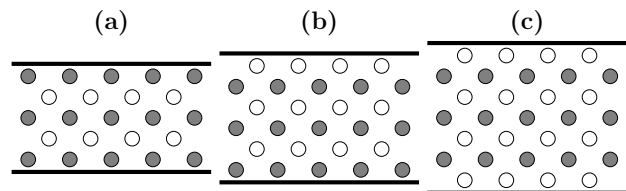


FIG. 14. Different boundary condition configurations. Gray (white) circles denote integer (half-integer) lattice sites.

The band diagrams corresponding to these edge configurations are shown in Fig. 15. Notice that Fig. 15(a) was considered in Sec. V B. The band diagrams displayed in Figs. 15(b-c) contain one (b) or two (c) rows of half-integer lattice sites. The most significant difference is the large number of edge eigenvalues that share frequencies with bulk modes in the frequency range $(0.448, 0.547)$. Two things that do not change with boundary conditions: (a) the presence of a unidirectional state located in the zone gap region of the diagram, and (b) the bulk bands.

The curvature and shape of the dispersion curves corresponding to edge modes have sensitive dependence on the boundary conditions (see also [19]). While the edge modes vary with boundary conditions, the bulk bands are found to be impervious to changes at the edges. Moreover the Chern numbers, calculated from the bulk bands, do not depend on the edges and with them the number of gapless edge states. Once a bulk band acquires a non-trivial Chern number, there will be a topological edge mode present even when defects along the boundary are introduced.

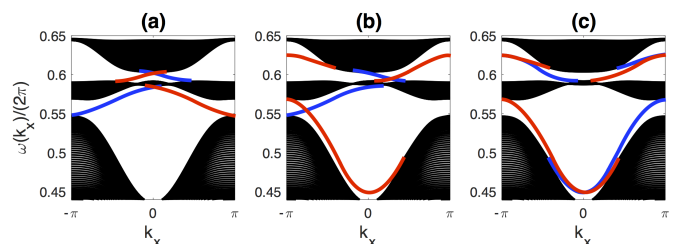


FIG. 15. (color online) Dispersion bands corresponding to the boundary conditions shown in Fig. 14, respectively. Red (blue) curves correspond to edge modes localized along the top (bottom) edge.

Appendix C: Improving the Tight-binding Approximation

A natural question to ask is how could the discrete model better approximate the system? One way to ac-

	p	1	2	3	4
\mathbf{d}_1	$\frac{\ \omega_{\text{num}}(\mathbf{k}) - \omega_{\text{disc}}(\mathbf{k})\ _{\text{max}}}{\ \omega_{\text{num}}(\mathbf{k})\ _{\text{max}}}$	36.62×10^{-2}	11.50×10^{-2}	2.96×10^{-2}	7.66×10^{-2}
	$\ \omega_{\text{disc}}(\mathbf{k}) - \omega_{\text{disc}}(-\mathbf{k})\ _{\text{max}}$	1.69×10^{-5}	1.09×10^{-4}	7.38×10^{-5}	8.50×10^{-5}
\mathbf{d}_2	$\frac{\ \omega_{\text{num}}(\mathbf{k}) - \omega_{\text{disc}}(\mathbf{k})\ _{\text{max}}}{\ \omega_{\text{num}}(\mathbf{k})\ _{\text{max}}}$	18.02×10^{-2}	3.31×10^{-2}	2.54×10^{-2}	2.85×10^{-2}
	$\ \omega_{\text{disc}}(\mathbf{k}) - \omega_{\text{disc}}(-\mathbf{k})\ _{\text{max}}$	1.56×10^{-5}	6.12×10^{-5}	2.76×10^{-5}	3.46×10^{-5}
\mathbf{d}_3	$\frac{\ \omega_{\text{num}}(\mathbf{k}) - \omega_{\text{disc}}(\mathbf{k})\ _{\text{max}}}{\ \omega_{\text{num}}(\mathbf{k})\ _{\text{max}}}$	8.42×10^{-2}	2.53×10^{-2}	2.39×10^{-2}	2.62×10^{-2}
	$\ \omega_{\text{disc}}(\mathbf{k}) - \omega_{\text{disc}}(-\mathbf{k})\ _{\text{max}}$	6.71×10^{-6}	2.89×10^{-5}	1.17×10^{-5}	1.39×10^{-5}

TABLE II. Comparison between discrete (disc) and numerical (num) spectral bands in Fig. 16. The max norm is defined by $\|f(\mathbf{k})\|_{\text{max}} \equiv \max_{\mathbf{k} \in BZ} |f(\mathbf{k})|$.

comply this is to increase the number of Wannier mode interactions. In Sec. V we computed the spectral bands and included all interactions with nearby Wannier modes whose center was a euclidean distance of one or less away. We can increase the number of interactions in the model for an overall better approximation of the problem, up to a point. On the other hand however, more interactions leads to a higher complexity and will become computationally expensive to solve. In Sec. V we opted for the fewest number of interactions that gave us a reasonable set of topological bands.

A comparison of the spectral bands for different numbers of Wannier mode interactions is shown in Fig. 16, where only the real part is shown. As the number of interactions increases, qualitatively the discrete approximation is found to improve. This improvement is quantified in Table II where the relative band error and the inversion symmetry error are given. Among the $p = 2, 3, 4$ bands, the relative max error is 11.5%, 3.3% and 2.6%, respectively, in Figs. 16(a), (b), and (c). The table also shows that all three cases have excellent preservation of inversion symmetry. We also point out that all three of these band configurations have the nontrivial Chern numbers shown in Fig. 6(b). Furthermore, when solved with edge boundary conditions, each set supports gapless edge modes that are topologically protected.

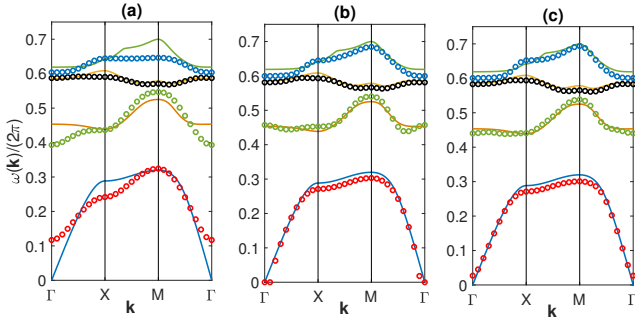


FIG. 16. The spectral bands over the irreducible Brillouin zone for (a) \mathbf{d}_1 , (b) \mathbf{d}_2 , and (c) \mathbf{d}_3 . Note that panel (a) is the same as Fig. 6(b)